Long-term, continuous, and multimodal monitoring of respiratory digital biomarkers via wireless epidermal mechano-acoustic sensing in clinical and home settings for COVID-19 patients

John Rogers (✉ jrogers@northwestern.edu)

Northwestern University   https://orcid.org/0000-0002-2980-3961

Xiaoyue Ni

Northwestern University   https://orcid.org/0000-0002-1822-1122

Wei Ouyang

Northwestern University

Hyoyoung Jeong

Querrey Simpson Institute for Bioelectronics   https://orcid.org/0000-0002-1808-7824

Jin-Tae Kim

Northwestern University

Andreas Tzavelis

Northwestern University

Ali Mirzazadeh

Georgia Institute of Technology

Changsheng Wu

Northwestern University

Jong Yoon Lee

Sibel Inc

Matthew Keller

Sonica Health

Chaithanya Mummidisetty

Shirley Ryan Ability Lab

Manish Patel

University of Illinois at Chicago   https://orcid.org/0000-0003-3835-9601

Nicholas Shawen

Shirley Ryan Ability Lab

Joy Huang

Northwestern University

Hope Chen

Northwestern University

Sowmya Ravi
Northwestern University

Jan-Kai Chang
Northwestern University

KunHyuck Lee
Northwestern University   https://orcid.org/0000-0002-9765-1541

Yixin Wu
Northwestern University   https://orcid.org/0000-0002-6315-4694

Ferrona Lie
Northwestern University

Youn Kang
Northwestern University   https://orcid.org/0000-0002-8433-5515

Jong Uk Kim
Sungkyunkwan University

Leonardo Chamorro
University of Illinois at Urbana-Champaign

Anthony Banks
Northwestern University

Ankit Bharat
Northwestern University

Arun Jayaraman
Northwestern University

Shuai Xu
Northwestern University

Article

1 **Long-term, continuous, and multimodal monitoring of respiratory digital biomarkers via wireless**

2 **epidermal mechano-acoustic sensing in clinical and home settings for COVID-19 patients**

3

4 Xiaoyue Ni[1,2,22], Wei Ouyang[1,22], Hyoyoung Jeong[1,22], Jin-Tae Kim[1], Andreas Tzavelis[1,3,4], Ali

5 Mirzazadeh[5], Changsheng Wu[1], Jong Yoon Lee[6], Matthew Keller[7], Chaithanya K. Mummidisetty[8], Manish

6 Patel[1,9], Nicholas Shawen[8], Joy Huang[10], Hope Chen[10], Sowmya Ravi[11], Jan-Kai Chang[1,12], Kun Hyuck

7 Lee[1,13], Yixin Wu[1], Ferrona Lie[1], Youn J. Kang[1], Jong Uk Kim[14], Leonardo P. Chamorro[15], Anthony R.

8 Banks[1], Ankit Bharat[16], Arun Jayaraman[8], Shuai Xu[1,17] and John A. Rogers[1,3,13,18,19,20,21]

9

10 [1]Querrey Simpson Institute for Bioelectronics, Northwestern University, Evanston, IL, USA

11 [2]Department of Mechanical Engineering and Materials Science, Duke University, Durham, NC, USA

12 [3]Department of Biomedical Engineering, Northwestern University, Evanston, IL, USA

13 [4]Medical Scientist Training Program, Feinberg School of Medicine, Northwestern University, Chicago, IL,

14 USA

15 [5]College of Computing, Georgia Institute of Technology, Atlanta, GA, USA

16 [6]Sibel Inc, Morton Grove, IL, USA

17 [7]Sonica Health, Niles, IL, USA

18 [8]Max Nader Lab for Rehabilitation Technologies and Outcomes Research, Center for Bionic Medicine,

19 Shirley Ryan Ability Lab, Chicago, IL, USA

20 [9]University of Illinois College of Medicine at Chicago, Chicago, IL, USA

21 [10]Feinberg School of Medicine, Northwestern University, Chicago, IL, USA

22 [11]Division of Thoracic Surgery, Feinberg School of Medicine, Northwestern University, Chicago, IL, USA

23 [12]Wearifi Inc., Evanston, IL, USA

24 [13]Department of Materials Science and Engineering, Northwestern University, Evanston, IL, USA

25 [14]School of Chemical Engineering, Sungkyunkwan University, Suwon, Republic of Korea

26 [15]Department of Mechanical Science and Engineering, University of Illinois at Urbana-Champaign,

27 Champaign, IL, USA

28 [16]Department of Surgery, Feinberg School of Medicine, Northwestern University, Chicago, IL, USA

[17]Department of Dermatology, Feinberg School of Medicine, Northwestern University, Chicago, IL, USA

[18]Department of Mechanical Engineering, Northwestern University, Evanston, IL, USA

[19]Department of Chemistry, Northwestern University, Evanston, IL, USA

[20]Department of Electrical Engineering and Computer Science, Northwestern University, Evanston, IL, USA.

[21]Department of Neurological Surgery, Northwestern University, Evanston, IL, USA

[22]These authors contributed equally: Xiaoyue Ni, Wei Ouyang, Hyoyoung Jeong

* E-mail: stevexu@northwestern.edu, jrogers@northwestern.edu

Capabilities in continuous monitoring of key physiological parameters of disease have never been more important than in the context of the global COVID-19 pandemic. Soft, skin-mounted electronics that incorporate high-bandwidth, miniaturized motion sensors represent a powerful class of technology for digital, wireless measurements of mechano-acoustic (MA) signatures of both core vital signs (heart rate, respiratory rate, and temperature) and underexplored biomarkers (coughing count) with high fidelity and immunity to ambient noises. Here, we introduce an effort that integrates such an MA sensor, a cloud data infrastructure and data analytics approaches based on digital filtering and convolutional neural networks for comprehensive monitoring of COVID-19 infections in sick and healthy individuals in a population, both in the hospital and the home. This hardware/software system extracts diverse signatures of health status in an automated fashion from a single device and time series data stream. Unique features are in quantitative measurements of coughing and other vocal events, as indicators of both disease and infectiousness. Systematic imaging studies demonstrate direct correlations between the time and intensity of coughing, speaking and laughing and the total droplet production, as an approximate indicator of the probability for disease spread. The sensors, deployed on COVID-19 patients along with healthy controls in both inpatient and home settings, record coughing frequency and intensity continuously, along with a comprehensive collection of other biometrics, with recording times for individuals of more than a month after disease diagnosis. These pilot studies include 3,111 hours of data spanning 363 days from 37 COVID-19 patients (20 females, 17 males) with 27,651 coughs detected in total along with continuous measurements of heart rate, respiratory rate, physical activity, and skin temperature. Manual labeling of randomly sampled 10,258 vocal events from 10 COVID-19 patients (6 females, 4 males) suggests a sensitivity of 0.87 and a specificity of 0.96 in cough detection using automated algorithms. The collective results indicate a decaying trend of coughing frequency and intensity through the course of disease recovery, but with wide variations across patient populations. The methodology also opens opportunities to study patterns in biometrics across individuals and among different demographic groups.

As of Nov. 1st, The Center for Disease Control's (CDCs) tabulations (https://covid.cdc.gov/covid-data-tracker/#cases_casesper100klast7days) indicate over 9 million recorded cases of COVID-19 and more than 229,000 in deaths in the U.S. The collective response to this global pandemic includes a mobilization of resources to diagnose, track, treat, and vaccinate against the SARS-CoV-2 virus that causes COVID-19. Accurate and widespread testing is a key component of this response[1]. Although the capacity and availability of COVID-19 molecular diagnostics continues to increase, experts still note significant shortcomings associated with high variabilities in accuracy of tests across manufacturers, constraints in key materials and supplies, long turnaround times associated with certain types of tests, inadequate access to testing sites and a lack of human resources[2]. The wide range of clinical presentations of infection with SARS-CoV-2 causes additional difficulties. In particular, SARS-CoV-2 often leads to asymptomatic or mild infections such that individuals can spread the disease prior to the demonstration of symptoms or positive molecular tests[3–5]. Although certain patient characteristics (e.g. age, male gender[6]) accompany severe disease, there remain limited prognostic tools to assess the trajectory of infection and the eventual need for hospitalization or mechanical ventilation. As an additional consideration, the CDC confirms that COVID-19 can be contracted via airborne transmission along with contact and droplet transmission — features that underscore the need to improve capabilities in risk stratification of exposures via contact tracing and to ensure sufficient quarantining for recovering individuals.

To address some of these needs, a wide range of digital health tools from mobile applications to collect self-reported patient symptoms to consumer wearable devices and clinical grade medical sensors are under development and in initial stages of deployment[7]. Early results show some promise. Researchers at FitBit (San Francisco, CA) report the ability to identify infection with COVID-19 via 4 previous days of data collected from their wrist-worn devices to yield overnight heart rate, respiratory rate, and heart rate variability in a cohort of 1,181 COVID-19 patients[8]. Others claim similar detection capabilities with alternative wrist-based devices[9]. Several ongoing large-scale trials aim to evaluate these wearables for early detection of COVID-19 infection, from smart rings (Oura Ring), skin-interfaced patches by VitalConnect (https://www.medicalcountermeasures.gov/newsroom/2020/vitalconnect/), Philips (https://www.usa.philips.com/a-w/about/news/archive/standard/news/press/2020/20200526-philips-

launches-next-generation-wearable-biosensor-for-early-patient-deterioration-detection-including-clinical-

surveillance-for-covid-19.html), Sonica

(https://www.medicalcountermeasures.gov/newsroom/2020/sonica/), to other smart watches (*e.g.*

Empatica) with support from various federal agencies

(https://www.medicalcountermeasures.gov/newsroom/2020/empatica/). While consumer-grade wearables

mount on the finger or wrist to monitor some subset of conventional vital signs[10–13], such as heart rate, the

mounting location, constrained to loose interfaces at the wrist or finger, fundamentally limits the range of

detectable physiological activities, particularly respiratory signals[14,15]. The inability to capture complex

health information reduces the potential of these technologies for precise and reliable analysis of

disease[16]. Development of robust metrics for early detection and disease tracking requires multimodal

operation to join across different digital biomarkers and to incorporate unconventional metrics closely

relevant to the disease of interest. Daunting challenges remain in addressing these wide-ranging

requirements simultaneously without sacrificing the simplicity and ease-of-use of the sensing system, as

necessary for practical deployment at scale in remote, continuous monitoring settings.[17]

As COVID-19 is predominately a respiratory disease, cough and other sounds from the thoracic cavity,

trachea and esophagus are examples of potentially useful but underexplored biometrics to identify,

monitor, and track recovery for this disease. Previous lab-scale studies demonstrate cough-based

diagnoses of diverse respiratory diseases through measurements of coughing frequency[18], intensity[19],

persistency[20], and unique coughing audio features[21]. Recent work applies voice profiling and computer

audition to track cough, speech, respiratory, and other sounds for risk assessment and diagnosis of

COVID-19 based on the distribution of symptoms (https://cvd.lti.cmu.edu, https://buildforcovid19.io/detect-

now/, https://www.covid-19-sounds.org/en/credits.html). Monitoring cough and other vocal events

(speaking, laughing, *etc.*) not only provides a signature of disease but also has potential in generating

metrics of infectiousness, as these mechanisms yield aerosols/droplets that contribute to virus

transmission[22–24]. Oral fluid particles with diameters of >5-10 μm are referred to as respiratory droplets;

diameters <5 μm in diameter are referred to as droplet nuclei, or aerosols (https://www.who.int/news-

room/commentaries/detail/transmission-of-sars-cov-2-implications-for-infection-prevention-precautions).

Previous studies show that the total volume of aerosols correlate with the loudness and duration of vocal events, such that measurements of the timing and intensity of sounds may serve as reliable metrics to quantify one aspect associated with risks of spreading the disease[25].

Point-of-care or semi-continuous methods for quantifying coughing or other vocal activities rely on techniques and devices such as electromyography, respiratory inductive plethysmography, accelerometers, microphones, or a combination of several sensors with other exploratory ones (*e.g.*, the nasal thermistor or the electrocardiography)[26–31]. Microphone-based approaches, especially those that use built-in microphones in smartphones, prevail due to their widespread availability and their alignment with large crowd-sourced datasets (*e.g.*, COUGHVID, HealthMode, DetectNow, VoiceMed). Data analysis approaches use digital signal processing of the resulting audio signals (*e.g.*, Fourier[32,33], Wavelet[34], Mel frequency cepstral coefficients (MFCCs)[32,35,36], RASTA-PLP spectrum or cepstrum[37]), often followed by machine learning algorithms (*e.g.*, Convolutional Neural Network[32,36], Recursive Neural Network[32], Time-Delay Neural Network[38], *k*-Nearest Neighbors[39,40], Hidden Markov Model[32,41], Random Forest[42], Support Vector Machine[32,35]) for further classification. A key challenge is that background sounds and/or environmental noises frustrate robust and accurate measurements in home settings, when implemented without rigorous guidelines or protocols. Also, and perhaps more importantly, audio recordings raise many serious privacy and prohibitive legal issues, thereby limiting the scale of application. In addition, measurements of loudness are highly unreliable because they depend strongly on the separation between the device and the subject, which is typically not well controlled.

The results presented here bypass these disadvantages, to allow continuous, accurate, and standardized assessments of respiratory biomarkers correlative to health status and droplet/aerosol production in naturalistic environments, with additional information on a broad range of traditional vital signs. Specifically, this paper presents a wireless, multimodal monitoring system that combines unusual hardware and software capabilities for continuously monitoring a breadth of conventional and unconventional physiological parameters of direct relevance to COVID-19, with additional potential for use across a wide variety of other diseases and conditions. The hardware component corresponds to a

soft, skin-integrated wireless device that mounts on the suprasternal notch for continuous recording of subtle motions associated with underlying body processes, each of which has unique mechanical or vibratory signatures. This mechano-acoustic (MA) device interfaces with a data analytics platform that combines digital signal filtering with convolutional neural networks to extract key features and insights from the recordings. Examples range from standard vital signs such as heart rate, respiration rate, body orientation and physical activities, to underexplored yet essential measurements of respiratory events such as coughing, speaking, laughing, throat clearing, singing, and sneezing that have been linked to patient health and/or COVID-19 transmission. The device captures these latter types of events without the use of a microphone, thereby bypassing privacy/security concerns as well as confounding effects of ambient noise. The results allow not only for detection of early signs of symptoms but also symptomatic progression of infected individuals through various stages of the disease, including responses to emerging therapeutics. Systematic studies using particle tracking velocimetry indicate that coughing, speaking, and laughing events measured with these devices also correlate to the total number of droplet production. This link offers an opportunity to continuously quantify the potential infectiousness of individuals, as critical information for healthcare workers in caring for particularly infectious COVID-19 patients and for better risk stratification in the context of contact tracing and individual quarantines. Pilot studies on COVID-19 patients at a large academic medical center (Northwestern Memorial Hospital) and a large rehabilitation hospital (Shirley Ryan Ability Lab) include 3,111 hours of data spanning a total of 363 days from 37 patients (20 females, 17 males), in an overall implementation that supports almost completely automated operation, with minimal user burden. The longest monitoring period corresponds to more than one month of recordings that capture both the inpatient, clinical, and post-discharging, home settings. This type of long-term monitoring reveal trends in various parameters, including coughing frequency, following the test-positive date for 8 patients (4 females, 4 males) over more than seven days. Evaluations across 27 patients (15 females, 12 males) with ages between 21 and 75 reveal diverse coughing patterns across individuals and consistent trends during the recovery process. A comparison of coughing frequency and coughing intensity among different demographic groups follows from a clustering of large number of events.

Results:

Sensor designs, system configurations, and wireless, cloud-enabled mode of operation. Figure 1a
presents a schematic illustration of the system configurations. The circuit architecture represents an
advanced version of the soft, skin-interfaced MA device reported previously[43]. Briefly, an open-
architecture, flexible printed circuit board (fPCB, 25-um-thick middle polyimide with double-sided 12-um-
thick rolled, annealed copper, AP7164R, DuPont) with serpentine conductive traces supports collections
of chip-scale components including a high-bandwidth, inertial measurement unit (IMU) with a tri-axial
accelerometer (LSMDSL, STMicroelectronics) as the key sensing element, a Bluetooth Low Energy (BLE)
system-on-a-chip for control and wireless connectivity, on-board memory module for data storage and a
wireless unit for recharging a compact battery. A thin, soft elastomer membrane (Ecoflex, 00-30, smooth-
on, 300-um) completely encapsulates the device as a compliant, non-irritating interface to the
suprasternal notch, supported by a thin, double-sided biomedical adhesive. The design of the system for
the studies reported here includes an automated user interface that almost entirely eliminates manual
operations, where the wireless charging platform itself serves as a hub to switch modes from recording to
data transfer. Specifically, the device remains in data acquisition mode when not on the charger. During
charging, the device automatically stops recording and starts transmitting data to a BLE-enabled device
such as a phone or a tablet with internet connectivity to a HIPPA-compliant cloud server. Algorithms
operating on the server deliver results to a graphical dashboard for feedback to health workers and/or
patients.

When interfaced to the suprasternal notch, the device captures subtle vibrations of the skin as signatures
of a wide range of physiological processes, continuously and robustly[43]. Figure 1b shows an example of
three-axis acceleration data recorded from an inpatient (female, age 53) wearing the device for 48 hours.
The sampling rate for motions perpendicular to the surface of the skin (z-axis) is 1666 Hz; the rates for
the x-axis (perpendicular to the axis of the neck) and y-axis (along the neck) are 416 Hz. Apart from the
clear difference in acceleration amplitudes during daytime and nighttime, the features in the data reveal
different processes and body mechanics during natural activities. Figure 1c shows time series
representations of sample events in two-minute windows. Features associated with coughing and

speaking include high-frequency components with significant amplitudes ($\sim 10^0$ g) along the z- and y-axis but small amplitudes ($\sim 10^{-1}$ g) along the x-axis. Physical activity induces comparatively large accelerations ($\sim 10^0$ g) along all axes. During the periods without such activities, subtle vital signals from respiratory and cardiac cycles are readily apparent, even in the raw data. Recordings during sleep can also yield body orientations and snoring events, including those that are both strongly and scarcely audible.

Algorithm development. The focus here is on extraction of different vocal and respiratory events from these raw data. Methods for determining other important parameters such as overall activity levels, heart rate, and respiration rate, can be found elsewhere[43]. In the context of monitoring COVID-19 symptoms, a particular interest is in identifying and tracking coughing events, in the presence of other MA signals. Figure 2 presents a scheme for data pre-processing that exploits time-frequency features to differentiate coughing from other common daily activities. Algorithm development uses recordings captured from ten healthy normal subjects in controlled experiments with a protocol (see Methods for details) that generate a large number of events of interest in various body postures. Figure 2a shows typical z-axis data from a representative experimental session. Each testing sequence begins and ends with three taps of the fingers on the device as time stamp markers. In between are consecutive 10 forced coughs, 10 laughing, 10 throat clearing events, 30-s of walking, 10 cycles of breathing, and more than 20-s of speaking. Figure 2b shows time series and spectrogram representations of such events, the latter of which uses Short Time Fourier Transform and a Hanning window with a width Δt = 0.4 s moving in time steps of δt = 0.01 s. The algorithm considers each windowed data independently in the process of cough determination. The coughing signals feature a broad-bandwidth impulse-like response, followed usually by a high-frequency chirp (> 200 Hz). Speaking signals also have high frequency components, but usually with distinct harmonic features. A previously established speaking detection algorithm based on such harmonics can screen the data for prominent speaking periods (Fig. 2c). After excluding speaking events identified in this manner, a minimum amplitude threshold P_{thrs} = -10,000 detects peaks of the logarithm of spectral power integrated across the high-frequency band (>10 Hz) (P_{MA}) and labels them as cough-like events, with a minimum time interval between peak events of 0.4 s (Fig. 2d). Here, cough-like events include laughing,

throat clearing, and also some speaking periods that exhibit unclear harmonics. Figure 2e shows the data processing flow, which begins with raw z-axis data and returns the time stamps for speaking and cough-like events, as well as their associated integrated logarithm power. Such an analysis applied to the testing data detects 26.4-s speaking with clear harmonics features, and identifies 10 coughing, 20 laughing, 12 throat clearing, 36 speaking, and 6 tapping instances as cough-like (Fig. 2a).

Distinguishing actual coughs from the pool of cough-like events calls for further classification by machine learning. A Convolutional Neural Network (CNN) uses as inputs Morlet Wavelet Transforms of 0.4-s raw z-axis data (shaped by the Hanning window) of these events (Fig. 3a). The Wavelet Transform offers advantages compared to the Short Time Fourier Transform for its favorable resolution in characterizing non-stationary signals, which improves the accuracy of classification. Fig. 3b shows scalograms of cough-like events, including tapping (one type of motion artifact), coughing, laughing, throat clearing, and speaking events. These scalograms, with shapes of 60 x 666 x 1, serve as inputs to the CNN model. As shown in Fig. 3c, the CNN starts with a 3-channel convolutional layer with a kernel size of 3 x 3, followed by a standard 50-layer Residual Neural Network (ResNet), a state-of-the-art CNN architecture for image classification[44]. The output of the ResNet flattens to a layer of 86,106 neurons, followed by 2 fully connected layers with Rectified Linear Unit (ReLU) activation and 2 dropout layers (p=0.5) alternately. The final fully connected layer of the CNN model has 5 neurons with Softmax activation, which corresponds to probabilities associated with the 5 types of events of interest: coughing, speaking, throat clearing, laughing, and motion artifact, where most of the motion artifacts are those events arising from physical contact on or around the device.

Data collected from 10 healthy volunteers yield well-labeled time windows consisting of 1379 coughing, 1441 speaking, 1313 laughing, 1423 throat-clearing, and 2890 motion-artifact events. Because sample events generated in controlled experiments can differ from those that occur naturally in uncontrolled settings, the training of the CNN model uses not only scalograms of labeled events from 10 healthy volunteers (Subjects # 1-10) but also 10 COVID-19 patients during natural daily behaviors (Subjects # 11-20). Determinations of ground truth from the patient data involve listening to soundtracks created from the

accelerometer data and then manually labeling the data (See *Methods* for code availability). Most of the events associated with coughing, speaking, and motion artifacts can be determined unambiguously. Difficulties arise in distinguishing between laughing, throat clearing, and certain periods of speaking, thereby leading to some level of uncertainty. Such manual analysis of data collected from 10 COVID-19 patients generates a total of 1405 coughing, 1449 speaking, 193 laughing, 210 throat-clearing, and 2905 motion-artifact events. Table S1 includes detailed demographic and data-collection information for all the training subjects.

The generalization performance of the CNN model represents a key metric for large-scale deployment and automated use. A common testing method relies on a leave-one-out strategy, where one leaves a subject out of the training set (19 subjects for training) and then tests the trained model on this subject. Iterations apply this approach to each of the 20 subjects. Each training set consists of a random collection of 80% of the labeled events from the 19 subjects, thereby leaving the remaining 20% for validation. The training uses an Adam optimization algorithm. Fig. 3d shows the averaged confusion matrix of 20 leave-one-out testing cycles. The model achieves accuracies of 0.90 ± 0.08 for coughing, 0.88 ± 0.1 for speaking, 0.79 ± 0.14 for throat clearing, 0.81 ± 0.14 for laughing, and 0.98 ± 0.02 for motion artifact. The classifications for throat clearing and laughing have comparatively lower average accuracies and higher standard deviations, simply because features of short-term segments of throat clearing and laughing signals can resemble those of speaking signals, as evidenced by the confusion matrix (Fig. 3d). Fig. 3e shows the overall 5-way classification accuracies on each subject using a model trained on the other 19 subjects. The minimum overall accuracy is 0.85 for all subjects. The Receiver Operation Characteristic (ROC) curve characterizes the trade-off between sensitivity and specificity in binary classification – varying the threshold of the cut-off probability at the final output layer generates ROC curves of each of the five types of events (coughing vs. non-coughing, speaking vs. non-speaking, *etc.*). Figure 3f. presents the macro-averaged ROC curves for each subject. The high Area Under the Curve (AUC) > 0.97 for all subjects indicates that the model achieves a good balance between sensitivity and specificity (See Tab. S2 for detailed information).

Mechano-acoustic sensing of droplet production. These algorithms allow robust identification of coughing events, for tracking of frequency, intensity and, in the future, detailed time dynamics (*i.e.*, effective sounds), in the context of early symptom detection as well as assessments of the progression of the disease and the response to various novel therapeutics. Another value of quantitative cough monitoring, as well as other forms of vocalization such as speaking, singing, shouting, *etc.*, is in the context of disease spread. Previous studies show that different types and volumes of vocal or respiratory-related events yield significantly different levels of aerosol production[25], with direct relevance to evaluating the risks of viral transmission. The devices and algorithms reported here provide unique capabilities. Figure 4a shows results that calibrate the high-frequency power P_{MA} associated with the z-axis acceleration component of the MA signals to measurements with a decibel meter P_{dB} in a quiet (background noise < 40 dB) environment for cases of coughing, speaking (repeating words 'terminator'), and laughing from a healthy normal subject (male, Asian, age 30). The results show a linear correlation $P_{MA} = p_1 P_{dB} + p_2$ for all three classes in the audible range of 55-85 dB, with $p_1 = 200\pm20$ dB^{-1}, $p_2 = -12000\pm1700$ dB^{-1} for coughing, $p_1 = 105\pm10$ dB^{-1}, $p_2 = -7000\pm700$ dB^{-1} for speaking, and $p_1 = 114\pm30$ dB^{-1}, $p_2 = -5800\pm1200$ dB^{-1} for laughing (Fig. S1).

Figure 4b-c shows the experimental setup of quantitative imaging studies (see *Methods* for details) that examine correlations between MA data and droplet production, with a focus on relationships between the total number of droplets and the intensities of coughing, speaking and laughing. The measurements include droplet dynamics captured via Particle Tracking Velocimetry (PTV, see *Methods* for details), power levels from the MA data (P_{MA}), and audio levels from a decibel meter (P_{dB}), all synced in time. Figure 4d-f shows a sequence of results from the MA sensor and the PTV analysis for coughing, speaking, and laughing, respectively, where markers indicate events correctly identified and classified by the automated algorithm. Figure 4g-i are images of coughing, talking, and laughing at the peak of corresponding marked boxes in Figure 4d-f. The PTV method tracks of individual particles in the Lagrangian frame of reference[45]. Figure 4j-l shows the detected particles with sizes indicated by the diameters of the grey circular symbols. As expected, the findings indicate that a larger number of droplets (determined across the investigation area of ~34 × ~17 cm^2, and with sizes r > 50 μm in the detectable

range) results from coughing (200-800 droplets) than speaking or laughing (10-200 droplets) at comparable decibel levels and time durations. More than 60% of droplets are smaller than 150 µm in radius for all measured respiratory activities (Fig. S2). Interpolated horizontal velocity contours from droplet trajectories indicate a large swirling motion for coughing, with positive velocity near the mouth and negative velocity in the bottom of the investigated area (Fig. 4j). Droplets show ballistic behavior for speaking and dispersive for laughing (Fig. 4k and l). Particularly, this ballistic behavior of droplets is a result of enhanced jet-like transport of the expelled airflow induced by the plosive sound[46]. Drastically different inertial particle dynamics occur depending on the size of droplets even within the same cycle. Specifically, small droplets linger in the air and respond to ambient flows. Large droplets travel at high velocities and are minimally influenced by flows, within a range investigated. Statistical analyses of the total number of droplets (N_d) of all measured respiratory activities at various audio levels appear in Fig. 4m,n, and o. The number of droplets exhibits some correlation to the audio dB level and the power intensity of the MA data, for all activities. Figure S3 and Supplementary Video 1 include additional results from the imaging analysis of droplet dynamics.

Long-term multimodal monitoring from a cohort of COVID-19 patients. Scaled deployment of the MA device and the ML algorithm on the clinical floor on COVID-19 patients, without difficulty or user or physician burden, illustrates the practical utility and readiness of these technologies in continuous, long-term (> 7 days) monitoring of a host of parameters relevant to patient status, not only coughing dynamics but also other forms of vocalization, along with heart rate, respiration rate, body orientation and overall activity. These pilot studies correspond to a total of 3,111 hours of data from 37 patients (20 females, 17 males; see SI for detailed demographic information) with 27,651 automatically detected coughs. Figure 5a shows data and analysis results for a representative one-hour session with a female patient. The CNN model, trained using a process that is blind to any of the patients described in this section, returns predicted classes for each cough-like event detected by the pre-processing step. Investigating the MA signal through the manual labeling process based on audio files provides reference labels for comparison. Statistical analysis, on a total of 10,258 randomly sampled events from 10 patients (6 females, 4 males; patient ID's listed in Tab. S1) with manual labels shows macro-averaged sensitivity (*i.e.*

recall) of >=0.87 specificity of >=0.96, and >=0.85 precision for coughing (N = 2785) and artifacts

detection (N = 2768) (Fig. 5b, Tab. S2). The sensitivity and precision for speaking (N = 2758), throat

clearing (N = 1212), and laughing (N = 735) are as low as 0.58, likely due in part to the ambiguities in

ground-truth labeling mentioned previously. Table S2 includes additional details on statistical analyses

with subject-specific information. Figure 5c presents results of coughing counts per five minutes in bars

and the associated coughing effort (*i.e.*, P_{MA}) in color. In general, the coughing frequency and intensity

peak in the morning, and distribute evenly throughout the day. Figure 5d presents a similar analysis of

speaking, with uniformly distributed speaking time and loudness (*i.e.*, P_{MA}) during daytime. Previously

reported algorithms applied to these same MA data streams yield other important parameters[43]. For

example, Figure 5e-g summarizes heart rate, respiration rate and physical activities, where the color-

coded intensity values correspond to peak amplitudes of cardiac signals in the frequency band 20-55 Hz

and root mean square values for low-passed respiration cycles in the band 0.1-1 Hz. Figure 6a-e present

this collective information (coughing counts, speaking time, heart rate, respiration rate, and physical

activity, and their associated intensity or amplitude) for the same patient over one month. Grey shaded

areas indicate periods when the patient is not wearing the device. As discussed previously, the data

collection is autonomous and largely burden free. The patient simply mounts the device on the skin using

a disposable adhesive and removes it for charging/data downloading. The same analysis has been

applied to a total of 27 patients (15 females, 12 males) whose data are not used in building the CNN

model. Figure S4-S20 shows the results for the 17 patients (9 females, 8 males; patient ID's listed in Tab.

S1) with a minimum of seven days of enrollment.

Figure 6f presents a time series plot for 8 patients (4 females, 4 males; patient ID's listed in Tab. S1) with

the date of a positive PCR test for COVID-19 reported, where the event of interest is coughing count

organized by days after the test. The results suggest a correlation between coughing frequency with the

gradual process of recovery, as might be expected. The significant variation in decay rates, however,

suggests individual-specific recovery and aerosolization potential. Figure 6g summarizes the age

distribution for the total of 27 testing patients. Figure 6h compares the histogram of coughing frequency of

these individuals, to reveal the diverse regularity of coughing across time. Figure 6i shows the coughing

frequency versus the average coughing intensity for all hourly measurements, clustered into four demographic groups (males with age < 55, males with age ≥ 55, females with age < 55, females with age ≥ 55). The available results suggest that females tend to cough more than males. Table S1 includes detailed demographic and data-collection information for all the testing patients. Further studies on an expanded patient population with detailed demographic information are, however, necessary.

Discussion:

This paper introduces an automated, low-burden hardware-software solution for sensing of broad, diverse health information of direct relevance to patient status, with a specific focus on underexplored respiratory biomarkers such as cough and their changes with COVID-19 disease state. Scaled studies indicate applicability to COVID-19 patients in both clinical and home settings. The approach relies on a soft, wireless sensing device placed on the suprasternal notch, to capture data that can be processed through a combination of digital filtering and machine learning techniques to separate and quantify different body processes. For behaviors that include high frequency information, such as speaking and coughing, a preprocessing method based on Fourier and Wavelet spectral analysis separates these events from others in continuous time series data streams. A trained CNN model yields a five-way classification probability matrix for coughing, speaking, laughing, throat clearing, and motion artifact. In addition to patient status, these data show promise in tracking droplet/aerosol production and, therefore, disease transmission related to cough and other expiratory events. An application of the automated algorithm to the in-field data from 10 patients, checked manually against converted audio files, reveals sensitivity of 0.87, specificity of 0.96, and precision of 0.85 for coughing identification.

These results set the foundations for capabilities in monitoring patient status through a range of both conventional and unconventional metrics, with cough as an example of a potentially important digital biomarker that can yield insights to complement those from analysis of traditional vital signals. Approaches similar to those reported here can be considered in strategies that extract additional information from specific forms of speech such as plosive consonants and vowels, that tend to carry aerosols and droplets over large distances, advanced assessments of coughing and respiratory sounds,

correlations between body positions and these activities, as well as coupled responses and timing

intervals between different events. Integrating optical modules and clinical-grade temperature sensors

into this same device platform will enable measurements of blood oxygenation and core body

temperature, without affecting the ability to simultaneously capture MA signals. Algorithms of the type

presented here are readily adaptable to such data streams, with immediate relevance to early detection,

patient care and disease management for COVID-19. Thus, a single device and analytics approach can

capture multimodal information with many possibilities in data fusion for precision healthcare, including

but not constrained to COVID-19[17,47,48]. Scaled, remote deployment of this platform will yield large

amounts of accessible biometric data, as the basis for predictive disease models, cost effective care of

patients, and containment of disease transmission.

Methods

Device design and components. FPCB schematic diagram and board layout were designed using

AUTODESK EAGLE (version 9.6.0) for a stretchable and bendable mechano-acoustic device.

Serpentine-shaped outlines connect three separated islands (main body, sensor, charging coil). A

summary of the bill of materials (BOM) for the device includes 0201 and 0402 inch footprints passive

components (resistors, capacitors, and inductors), 4 turns of wireless charging coil pattern (resonance

frequency: 13.56 MHz), Full-bridge rectifier, power management IC (Bq25120a, Texas Instruments), 3.0V

step-down power converter (TPS62740, Texas Instruments), 3.7V lithium polymer battery (75 mAh),

voltage and current protection IC for Li-Polymer battery (BQ2970, Texas Instruments), BLE SoC

(nRF52840, Nordic Semiconductor), NAND flash memory (MT29F4G, Micron), and inertial measurement

unit (LSM6DSL, STMicroelectronics).

Device fabrication and encapsulation. Panels of FPCB were manufactured and surface-mount device

(SMD) processes were performed by an ISO 9001-compliant manufacturer. Customized firmware was

downloaded by Segger Embedded Studio, followed by an FPCB folding and battery soldering process.

Each aluminum mold for top and bottom layers was prepared with a freeform prototyping machine

(Roland MDX 540), and the devices were encapsulated using pre-cured top and bottom Layers (Silbione-

4420, each 300um thick) after filling silicone elastomer (Eco-Flex 0030, 1:1 ratio) in the cavity in which the device was positioned. After fixing and pressing top/bottom molds using clamps, the mold was placed into an oven that holds a temperature of 95 °C for 20 minutes to cure the silicone elastomer. The mold was then taken out of the oven and placed under the room temperature area for 20 minutes to cool to room temperature. Next, the clamps were removed, and the encapsulated device was placed on a cutting surface and excess enclosure material was removed using a pre-fabricated hand-held die cutter. A CO_2 laser formed the shape of the double-sided adhesives and yielded a smooth and clean contour cut.

Data collection. All the participants provided written/verbal consent prior to their participation in this research study (See Tab. S1 for demographic information of all individuals studied). Study procedures were approved by the Northwestern University Institutional Review Board (NU-IRB), Chicago, IL, USA (STU00202449 and STU00212522) and was registered on ClinicalTrials.gov (NCT02865070, NCT04393558). All study related procedures were carried in accordance with the standards listed in the Declaration of Helsinki,1964. During the study, participants wore an MA device at SN (Fig. 1a). In case of patients, a clinician/research staff assisted in placing the sensor.

Healthy controls were asked to perform 18 repetitions of the following sequence of activities with some variability in the intensity of each of the activities over a 2 to 4-hour period: 3 taps on the sensor, 10 coughs, 10 laughs, 10 throat clearings, 30-s of walking, 10 cycles of breathing (inhale and exhale), more than 20-s of speaking, and 3 taps on the sensor. Of these repetitions, sedentary activities in 5 sets were performed while sitting, 5 during standing and 8 while lying down (2 in supine, 2 in prone, 2 in left recumbent and 2 in right recumbent) positions. In the case of patients, a reduced set of activities were used at the beginning of each test, which included 3 taps on the sensor, 5 coughs, 5 cycles of deep breathing, and 3 taps on the sensor.

Sterilization process. After each use, MA sensor was thoroughly disinfected/ cleaned with isopropyl alcohol (70% or above) or Oxivir® TB wipes (0.5% hydrogen peroxide) and left to dry at room temperature and the same process is repeated twice.

Convolutional neural network. The CNN starts with a convolution with a kernel size of 3x3 and 3 different kernels, followed by a standard 50-layer residual neural network as descried in detail in ref. [44]. At the output of the residual neural network, a flattening layer of 86,106 neurons follows. Finally, 3 fully interconnected layers with 512, 128, and 5 neurons, respectively, and 2 dropout layers with p=0.5 follow alternately. The CNN uses an Adam optimizer for training. The training process follows a leave-one-out strategy, where one leaves a subject out of the training set (19 remaining subjects for training) and then tests the trained model on this subject. Each training set applies a 5-fold cross-validation procedure. This approach iterates through each of the 20 subjects. Table S2 includes detailed information on the cross-validation results for each subject.

Data analytics. All analysis used Python 3.0 with SciPy, PyWavelets, and TensorFlow packages.

Code availability. The codes used for audio soundtrack conversion and manual labeling process are available on GitHub at https://github.com/nixiaoyue/MA-cough. The analysis codes used in this study are available from the authors upon request.

Droplet dynamics via Particle Tracking Velocimetry (PTV). Droplet dynamics of coughing, speaking and laughing were quantified by PTV. Coughing, speaking (the word "terminator" was used) and laughing were repeated for 14, 26 and 15 times at various dB levels, respectively. More data sample for speaking was collected to cover a wider range of dB up to 100 dB. Each respiratory activity was performed in the customized box made of acrylic glass with the inner dimension of $45 \times 30 \times 30$ cm^3 (L×W×H). The investigation area for tracking droplets was ~34 × ~17 cm^2 illuminated by 16 arrays for 600 lumen led light bars. PTV experiments were recorded by a 2048 × 1088 Emergent HT-2000M with 50mm F1.4 manual focus Kowa lens at the frame rate of 338 fps. To achieve continuous and simultaneous measurements with ADAM sensor and audio meter (Decibel x calibrated by SD-4023 sound level meter and R8090 Sound Level Calibrator), approximately 10,000 frames were recorded for each respiratory activity. Preprocessing, calibration, tracking, and postprocessing are performed by the PTV code developed by the RETEG group at UIUC[45]. Image sequences were preprocessed by subtracting the background noise

and enhancing the contract. Droplets are detected in a sub-pixel level with the area estimation. The

scattering cross section of a detected droplet, refractive index of droplet as well as the surrounding

medium, air, and wavelength of the light source were used to calculate the actual radius of detected

droplets based on the Mie Scattering theory[49,50]. The minimum radius of droplets measured in this work is

~60 μm. Detected droplets were tracked using the Hungarian algorithm and linked by performing a five-

frame gap closing to produce longer trajectories. Velocity and Lagrangian acceleration were filtered and

computed using fourth-order B splines. vector contour fields were obtained by interpolating scattered

Langraigan flow particles at each frame based on the natural neighbor interpolation method[51].

References

1.   West, C. P., Montori, V. M. & Sampathkumar, P. COVID-19 testing: the threat of false-negative

      results. in *Mayo Clinic Proceedings* **95**, 1127–1129 (Elsevier, 2020).

2.   Pettit, S. D. *et al.* 'All In': a pragmatic framework for COVID-19 testing and action on a global

      scale. *EMBO Mol. Med.* **12**, e12634 (2020).

3.   Bai, Y. *et al.* Presumed asymptomatic carrier transmission of COVID-19. *Jama* **323**, 1406–1407

      (2020).

4.   Day, M. Covid-19: four fifths of cases are asymptomatic, China figures indicate. *Br. J. Med.* m1375

      (2020).

5.   Gandhi, M., Yokoe, D. S. & Havlir, D. V. Asymptomatic transmission, the Achilles' heel of current

      strategies to control COVID-19. *N. Engl. J. Med.* 2158–2160 (2020).

6.   Jordan, R. E., Adab, P. & Cheng, K. K. Covid-19: risk factors for severe disease and death. *Br. J.*

      Med. m1198 (2020).

7.   Menni, C. *et al.* Real-time tracking of self-reported symptoms to predict potential COVID-19. *Nat.*

      Med. **26**, 1037–1040 (2020).

8.   Natarajan, A., Su, H.-W. & Heneghan, C. Assessment of physiological signs associated with

      COVID-19 measured using wearable devices. *medRxiv* (2020). doi:10.1101/2020.08.14.20175265

9.   Miller, D. J. *et al.* Analyzing changes in respiratory rate to predict the risk of COVID-19 infection.

      medRxiv (2020). doi:10.1101/2020.06.18.20131417

10. Mishra, T. *et al.* Early Detection Of COVID-19 Using A Smartwatch. *medRxiv* (2020). doi:10.1101/2020.07.06.20147512

11. Greenhalgh, T., Koh, G. C. H. & Car, J. Covid-19: A remote assessment in primary care. *Br. J. Med.* **368**, (2020).

12. Hassantabar, S. *et al.* CovidDeep: SARS-CoV-2/COVID-19 Test Based on Wearable Medical Sensors and Efficient Neural Networks. *arXiv* (2020).

13. Hemphill, N. M., Kuan, M. T. Y. & Harris, K. C. Reduced Physical Activity During COVID-19 Pandemic in Children With Congenital Heart Disease. *Can. J. Cardiol.* **36**, 1130–1134 (2020).

14. Liu, H. *et al.* Comparison of different modulations of photoplethysmography in extracting respiratory rate: from a physiological perspective. *Physiol. Meas.* 41 (2020).

15. Karlen, W., Raman, S., Ansermino, J. M. & Dumont, G. A. Multiparameter respiratory rate estimation from the photoplethysmogram. *IEEE Trans. Biomed. Eng.* **60**, 1946–1953 (2013).

16. Jeong, H., Rogers, J. A. & Xu, S. Continuous on-body sensing for the COVID-19 pandemic: Gaps and opportunities. *Sci. Adv.* **6**, eabd4794 (2020).

17. Gravina, R., Alinia, P., Ghasemzadeh, H. & Fortino, G. Multi-sensor fusion in body sensor networks: State-of-the-art and research challenges. *Inf. Fusion* **35**, 1339–1351 (2017).

18. Loudon, R. G. & Brown, L. C. Cough frequency in patients with respiratory disease. *Am. Rev. Respir. Dis.* **96**, 1137–1143 (1967).

19. Pavesi, L., Subburaj, S. & Porter-Shaw, K. Application and validation of a computerized cough acquisition system for objective monitoring of acute cough: A meta-analysis. *Chest* **120**, 1121–1128 (2001).

20. Cloutier, M. M. & Loughlin, G. M. Chronic cough in children: A manifestation of airway hyperreactivity. *Pediatrics* **67**, 6–12 (1981).

21. Bales, C. *et al.* Can machine learning be used to recognize and diagnose coughs? *arXiv* (2020).

22. Zayas, G. *et al.* Cough aerosol in healthy participants: Fundamental knowledge to optimize droplet-spread infectious respiratory disease management. *BMC Pulm. Med.* **12**, (2012).

23. Mittal, R., Ni, R. & Seo, J. H. The flow physics of COVID-19. *J. Fluid Mech.* **894**, (2020).

24. Dbouk, T. & Drikakis, D. On coughing and airborne droplet transmission to humans. *Phys. Fluids*

32, (2020).

25.   Gregson, F. K. A. *et al.* Comparing the Respirable Aerosol Concentrations and Particle Size

         Distributions Generated by Singing , Speaking and Breathing. *ChemRxiv* **2**, 1–27 (2020).

26.   Fontana, G. A., Pantaleo, T., Lavorini, F., Boddi, V. & Panuccio, P. A noninvasive

         electromyographic study on threshold and intensity of cough in humans. *Eur. Respir. J.* **10**, 983–

         989 (1997).

27.   Drugman, T. *et al.* Audio and contact microphones for cough detection. in *13th Annual Conference

         of the International Speech Communication Association 2012, INTERSPEECH 2012* **2**, 1302–

         1305 (2012).

28.   Drugman, T. *et al.* Objective study of sensor relevance for automatic cough detection. *IEEE J.

         Biomed. Heal. Informatics* **17**, 699–707 (2013).

29.   Jasmine, A. & Jayanthy, A. K. Sensor-based system for automatic cough detection and

         classification. *Test Eng. Manag.* **83**, 13826–13834 (2020).

30.   Bush, A. Diagnostic and Therapeutic Methods - A New Device for Ambulatory Cough Recording.

         Hear. Lung **186**, 178–186 (1994).

31.   Elfaramawy, T., Latyr Fall, C., Morissette, M., Lellouche, F. & Gosselin, B. Wireless respiratory

         monitoring and coughing detection using a wearable patch sensor network. in *Proceedings - 2017

         IEEE 15th International New Circuits and Systems Conference, NEWCAS 2017* 197–200 (2017).

         doi:10.1109/NEWCAS.2017.8010139

32.   Amoh, J. & Odame, K. Deep neural networks for identifying cough sounds. *IEEE Trans. Biomed.

         Circuits Syst.* **10**, 1003–1011 (2016).

33.   Pramono, R. X. A., Imtiaz, S. A. & Rodriguez-Villegas, E. Automatic cough detection in acoustic

         signal using spectral features. in *2019 41st Annual International Conference of the IEEE

         Engineering in Medicine and Biology Society (EMBC)* 7153–7156 (IEEE, 2019).

34.   Kosasih, K., Abeyratne, U. R., Swarnkar, V. & Triasih, R. Wavelet augmented cough analysis for

         rapid childhood pneumonia diagnosis. *IEEE Trans. Biomed. Eng.* **62**, 1185–1194 (2014).

35.   Di Perna, L. *et al.* An automated and unobtrusive system for cough detection. in *2017 IEEE Life

         Sciences Conference (LSC)* 190–193 (IEEE, 2017).

36. Miranda, I. D. S., Diacon, A. H. & Niesler, T. R. A comparative study of features for acoustic cough detection using deep architectures. in *2019 41st Annual International Conference of the IEEE Engineering in Medicine and Biology Society (EMBC)* 2601–2605 (IEEE, 2019).

37. Wang, H.-H., Liu, J.-M., You, M. & Li, G.-Z. Audio signals encoding for cough classification using convolutional neural networks: A comparative study. in *2015 IEEE International Conference on Bioinformatics and Biomedicine (BIBM)* 442–445 (IEEE, 2015).

38. Amrulloh, Y. A., Abeyratne, U. R., Swarnkar, V., Triasih, R. & Setyati, A. Automatic cough segmentation from non-contact sound recordings in pediatric wards. *Biomed. Signal Process. Control* **21**, 126–136 (2015).

39. Monge-Álvarez, J., Hoyos-Barceló, C., Lesso, P. & Casaseca-de-la-Higuera, P. Robust detection of audio-cough events using local Hu moments. *IEEE J. Biomed. Heal. informatics* **23**, 184–196 (2018).

40. Hoyos-Barcelo, C., Monge-Alvarez, J., Shakir, M. Z., Alcaraz-Calero, J.-M. & Casaseca-de-La-Higuera, P. Efficient k-NN implementation for real-time detection of cough events in smartphones. *IEEE J. Biomed. Heal. informatics* **22**, 1662–1671 (2017).

41. Teyhouee, A. & Osgood, N. D. Cough Detection Using Hidden Markov Models. in *International Conference on Social Computing, Behavioral-Cultural Modeling and Prediction and Behavior Representation in Modeling and Simulation* 266–276 (Springer, 2019).

42. Larson, E. C., Lee, T., Liu, S., Rosenfeld, M. & Patel, S. N. Accurate and privacy preserving cough sensing using a low-cost microphone. in *Proceedings of the 13th international conference on Ubiquitous computing* 375–384 (2011).

43. Lee, K. H. *et al.* Mechano-acoustic sensing of physiological processes and body motions via a soft wireless device placed at the suprasternal notch. *Nat. Biomed. Eng.* **4**, 148–158 (2020).

44. He, K., Zhang, X., Ren, S. & Sun, J. Deep residual learning for image recognition. in *Proceedings of the IEEE conference on computer vision and pattern recognition* 770–778 (2016).

45. Kim, J. T., Nam, J., Shen, S., Lee, C. & Chamorro, L. P. On the dynamics of air bubbles in Rayleigh-Bénard convection. *J. Fluid Mech.* (2020). doi:10.1017/jfm.2020.148

46. Abkarian, M., Mendez, S., Xue, N., Yang, F. & Stone, H. A. Speech can produce jet-like transport

relevant to asymptomatic spreading of virus. *Proc. Natl. Acad. Sci. U. S. A.* **117**, 25237–25245 (2020).

47. Lahat, D., Adali, T. & Jutten, C. Multimodal Data Fusion: An Overview of Methods, Challenges, and Prospects. *Proceedings of the IEEE* **103**, 1449–1477 (2015).

48. Kumari, P., Mathew, L. & Syal, P. Increasing trend of wearables and multimodal interface for human activity monitoring: A review. *Biosensors and Bioelectronics* **90**, 298–307 (2017).

49. Bohren, C. F. & Huffman, D. R. *Absorption and scattering of light by small particles*. (John Wiley & Sons, 2008).

50. Schäfer, J., Lee, S.-C & Kienle, A. Calculation of the near fields for the scattering of electromagnetic waves by multiple infinite cylinders at perpendicular incidence. *J. Quant. Spectrosc. Radiat. Transf.* **113**, 2113–2123 (2012).

51. Kim, J.-T. & Chamorro, L. P. Lagrangian description of the unsteady flow induced by a single pulse of a jellyfish. *Phys. Rev. Fluids* **4**, 64605 (2019).

Acknowledgements

Author contributions
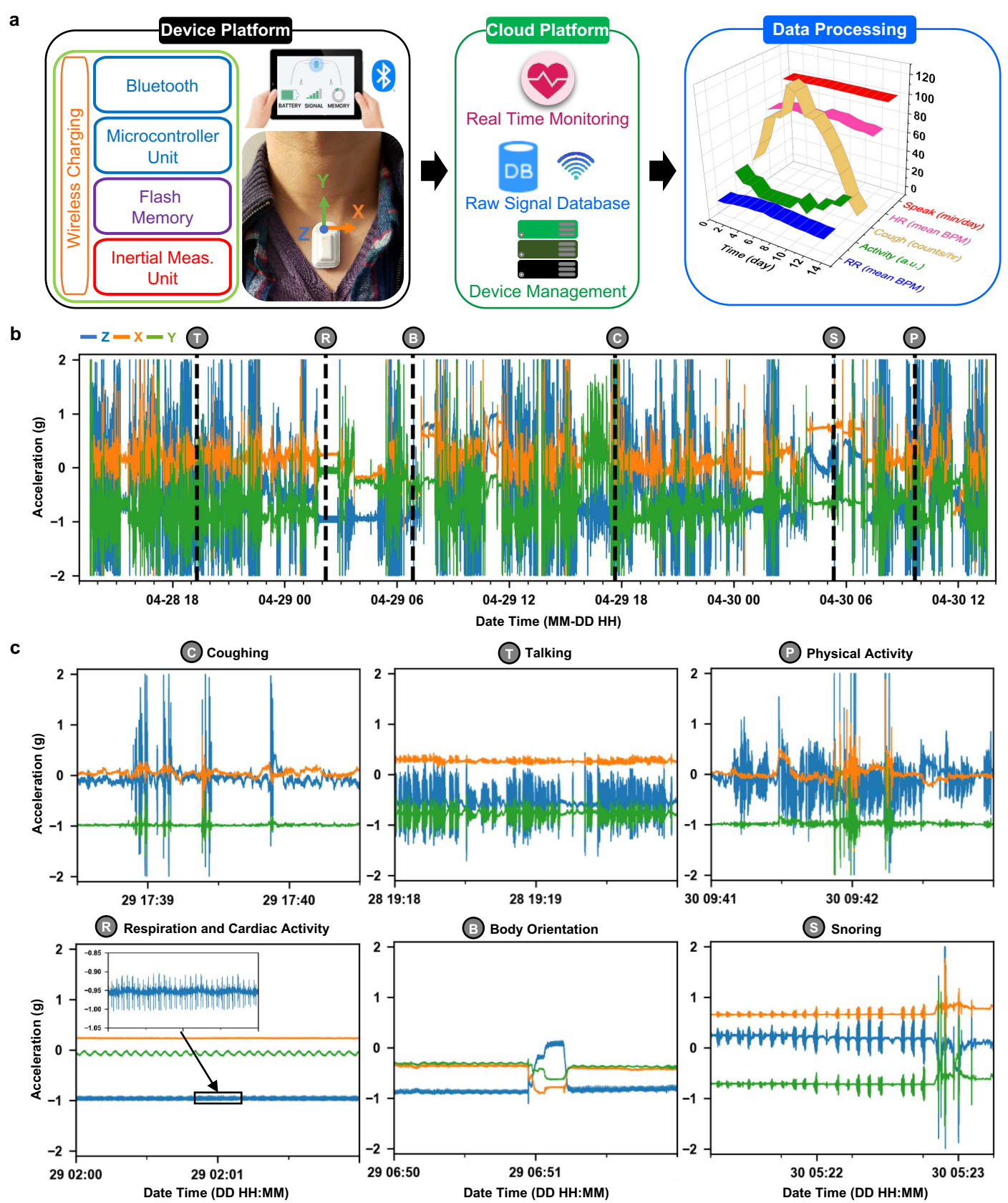
A.R.B, A.B, A.J., S.X., J.A.R. conceived and supervised the research project; X.N., W.O., A.T., developed the algorithm; H.J., J.Y.L., M.K., J.-K.C., K.H.L., J.U.K., A.R.B., and J.A.R. developed the hardware and cloud platform; X.N., W.O., A.T., A.M., C.W., J.H., H.C., S.R., K.B., Y.W., F.L., Y.J.K. analyzed the data; J.-K.C., K.H.L., K.M., M.P., N.S., A.R.B., A.B., A.J., and J.A.R. managed and deployed devices in hospitals and homes; J.T.K., L.P.C., and J.A.R. designed and conducted the aerosol imaging; X.N., W.O., H.J., J.T.K., S.X., and J.A.R. wrote the manuscript.
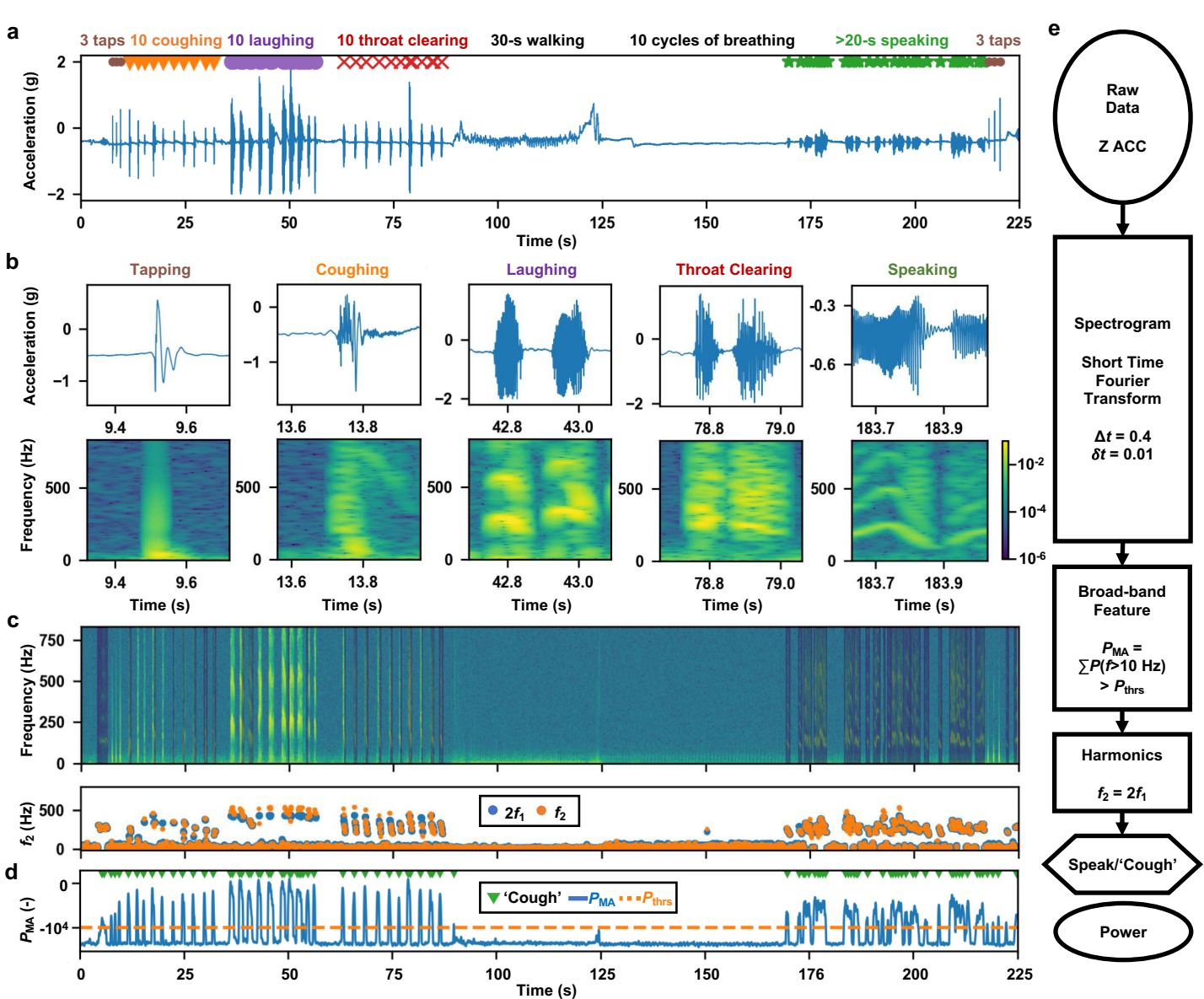
Competing interests

X.N, H.J, J.Y.L, K.H.L, A.J, S.X., and J.A.R. report inventorships and potential royalties in patents assigned to Northwestern University. M.K., and J.Y.L are employees of small private company with a commercial interest in the technology. A.R.B., S.X., and J.A.R. report equity ownership in a small private company with a commercial interest in the technology.
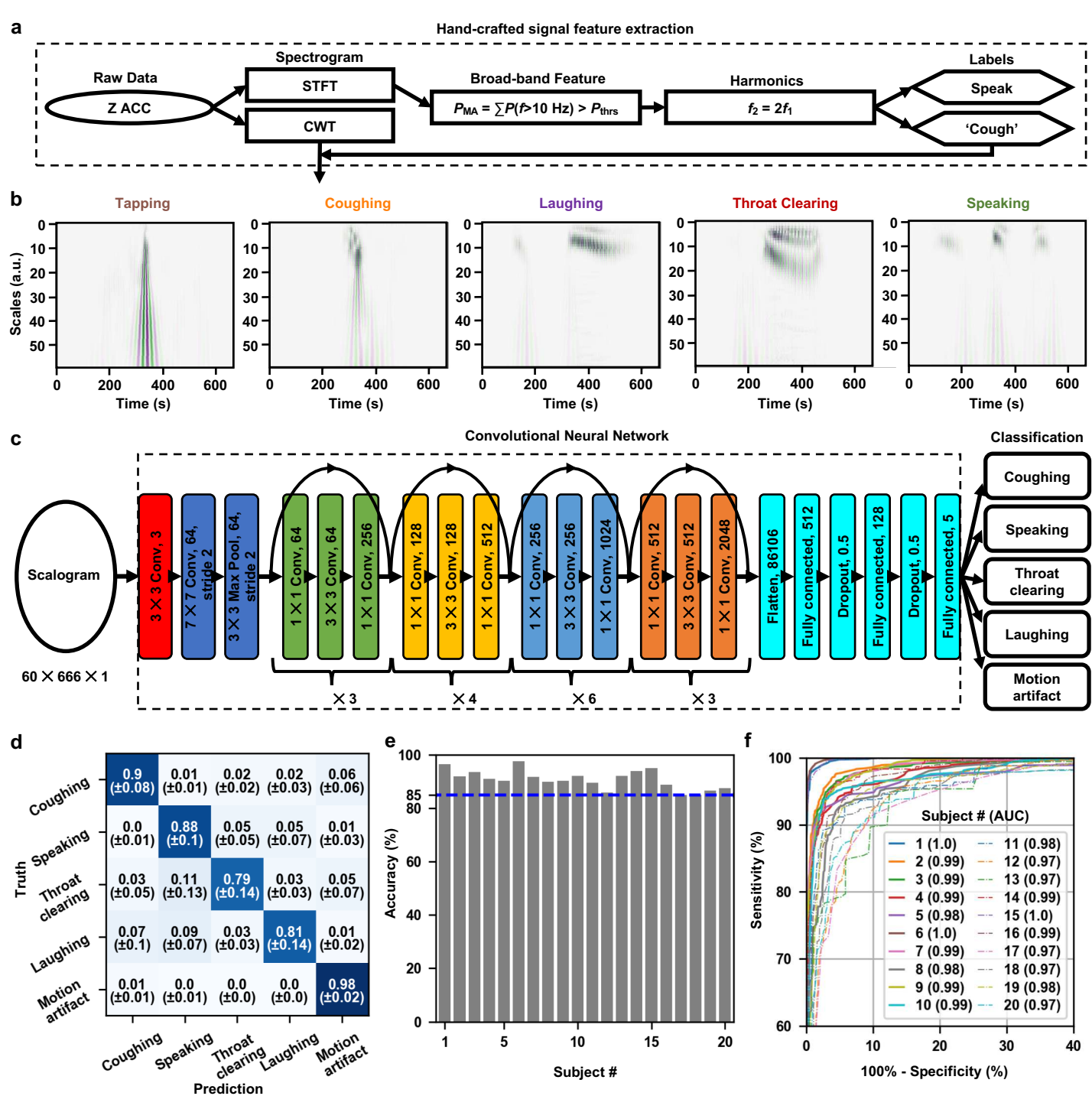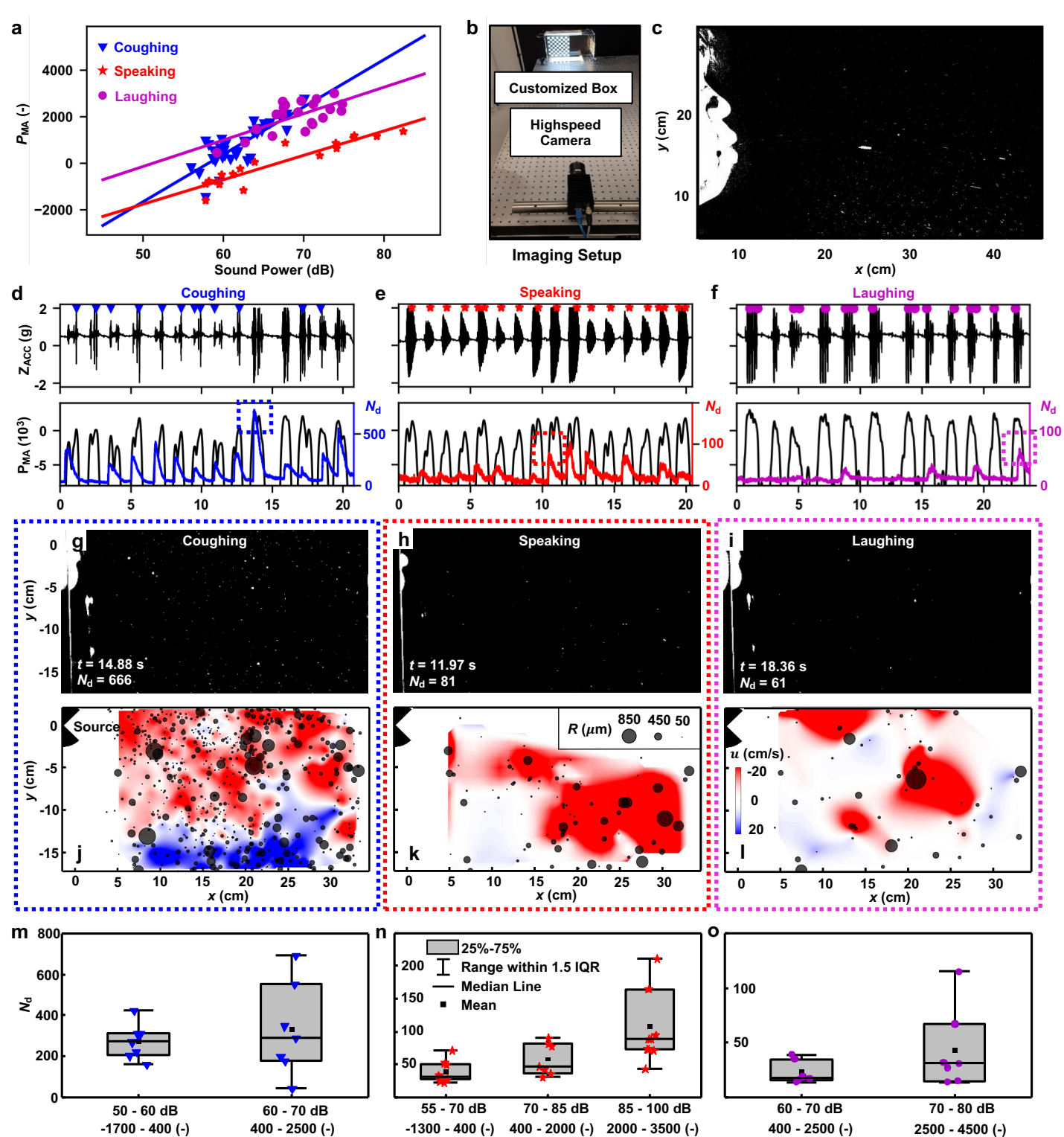
Figure 1. The health monitoring system incorporating a mechano-acoustic (MA) sensor, Bluetooth and cloud-based data transmission, automated data-processing platform and a user-interface with a minimum request for manual operation. (a) Schematics of the operational flow of the system that consists of a device, cloud, and data processing platforms. (b) Sample three-axis acceleration raw data acquired continuously over 48 hours on a COVID-19 patient. Dashed lines indicate occurrences of various representative body processes of interest, shown in (c) zoomed-in two-minute windows.
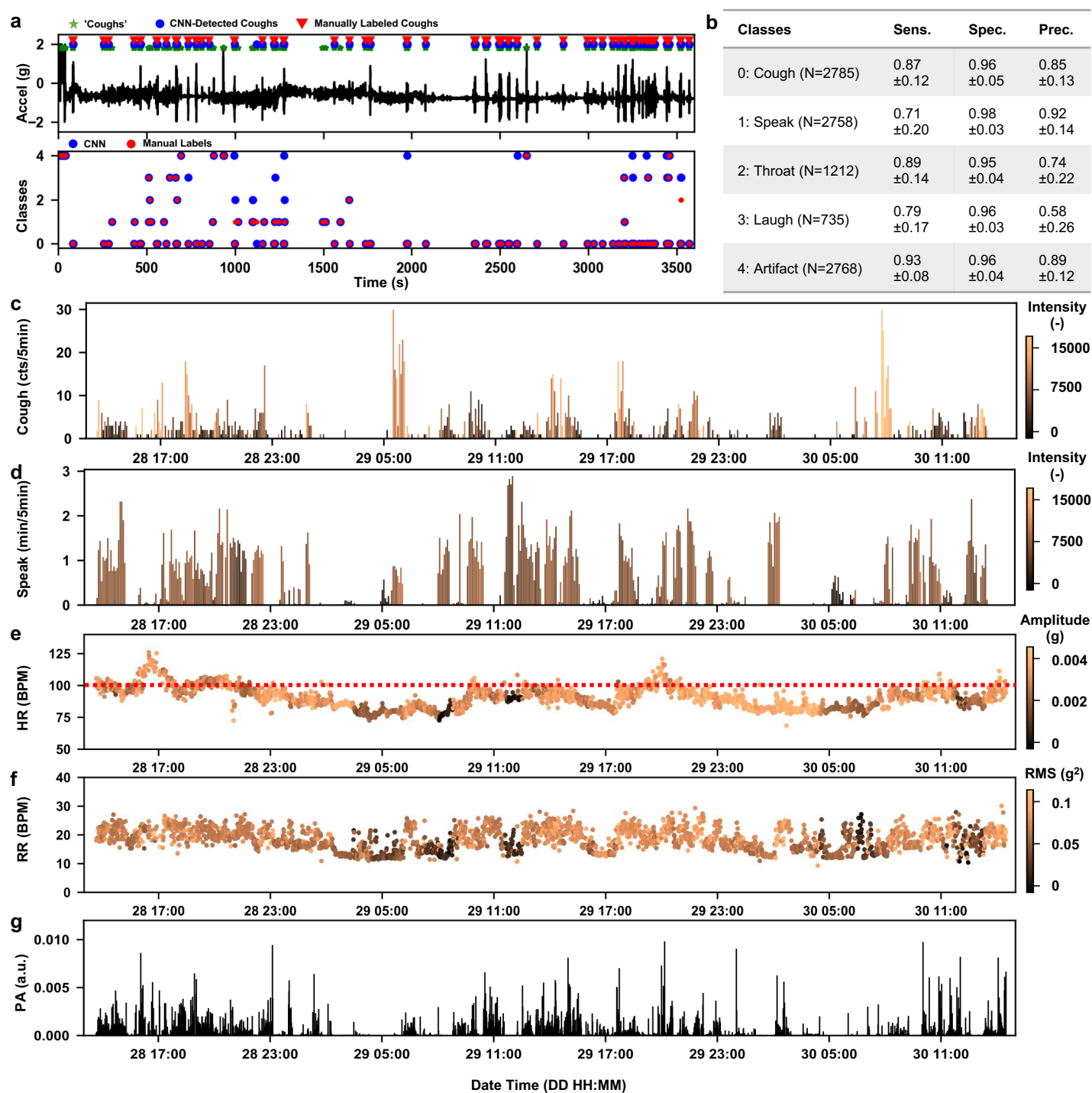
Figure 2. The signal preprocessing steps that identify broadband events of interest from the quiet and speaking time from mechano-acoustic (MA) measurements. (a) The raw z-axis data generated from controlled experiments on healthy normal subjects, with all the events of interest repeated in sequence following a designed protocol (See *Methods* for details). (b) Example 400-ms clips of the raw z-axis data and their corresponding spectrogram features. (c) Speaking signals distinct with a clear presence of harmonics ($P(f_1)$ and $P(f_2)$) of fundamental frequencies f_1 in the spectrogram analysis $P(f)$, where $2f_1 \approx f_2$; See Ref. 43 for details). Detected speaking periods are shaded in blue in the spectrogram. (d) After excluding speaking time, the detection of the high-frequency ($f > 10$ Hz) MA power peaks with a minimum time interval of 0.4 s and a threshold of -10000 yields time stamps for cough-like events that feature the impulse-like broad-band acoustics. (e) A flow diagram summarizing the preprocessing steps that take in the raw z-axis data and outputs the time stamps for cough-like and speaking events, along with their MA power, P_{MA}.
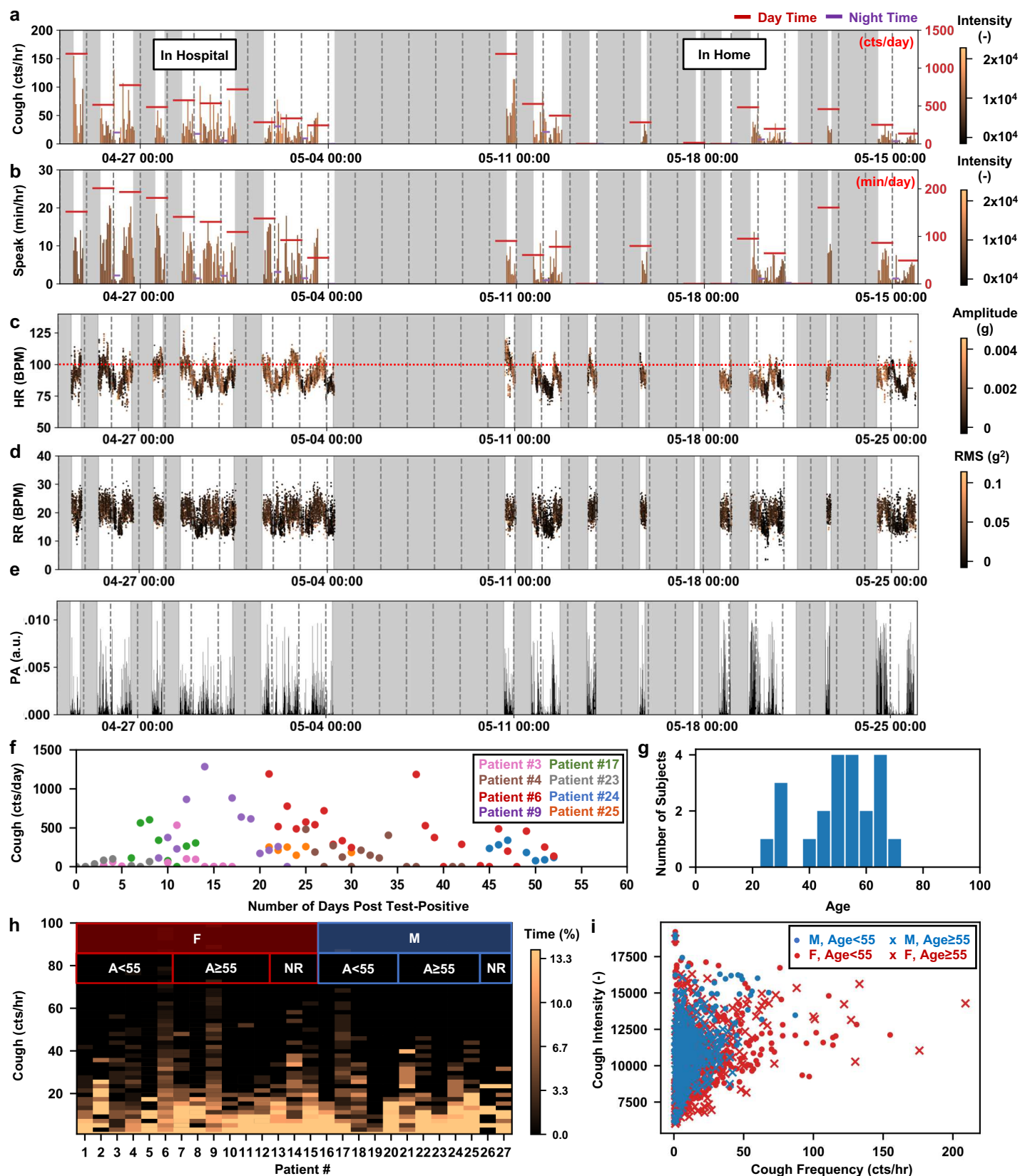
Figure 3. The machine learning algorithm for the classification of cough-like events extracted by the preprocessing algorithm. (a) Steps of feature scalogram generation from raw data. (b) Representative scalograms of events of interest. (c) The architecture of a convolutional neural network that takes in a feature scalogram and outputs its probabilities of classes. (d) The averaged confusion matrix from the iterated 20 leave-one-out testings. (e) The overall testing accuracy on each left-out subject using a model trained on the other 19 subjects. (f) The macro-averaged Receiver Operating Characteristic (ROC) curves of each left-out subject using a model trained on the other 19 subjects and the corresponding Area under the Curve (AUC).

Figure 4. Mechano-acoustic sensing to quantify the transmission of droplets. (a) MA power vs. decibel meter measurement for coughing, speaking, and laughing. (b) Experimental setup for optical imaging of droplets. (c) Sample image of coughing. (d,e,f) Time series of MA z-axis data in sync with the analysis of MA power and the imaging detection of the number of the particles. (g,h,i) Instantaneous images of coughing, talking, and laughing at the peak of corresponding marked boxes in d,e,f. (j,k,l) Detected particles with sizes indicated by the diameters of the grey circular symbols, overlapped with velocity contour fields at the corresponding instances in g,h,i; the color denotes streamwise velocity in horizontal (x-axis) direction. (m,n,o) Box and whisker plots showing the number of particles for all measured cycles of coughing, speaking, and laughing, respectively. See *Methods* section for full description.

Figure 5. Deployment of MA device to the in-field COVID-19 patients. (a) Example one-hour raw z-axis acceleration data measured from a female patient. The automated algorithm detects cough-like events and outputs five-way classification for the events to coughing (0), speaking (1), throat clearing (2), laughing (3), and motion artifacts (4). (b) The macro-averaged testing performance (sensitivity/recall, specificity, and precision) of each type of events on the 10 patients with manual labels, which include 10,258 randomly sampled events in total. (c,d) Example results of the detected coughing and talking frequency and intensity (color-coded) in five-minute windows from continuous 48-hour monitoring of the same patient (raw acceleration data are shown in Fig. 1b-c). (e,f,g) The vital information, *i.e.,* heart rate (HR), respiration rate (RR), and physical activity (PA), extracted from the same measurement, with their amplitude information color-coded.

Figure 6. Long-term monitoring of coughing and other biometrics of COVID-19 patients. Long-term mechano-acoustic sensing of (a) cough frequency per hour, (b) talk time per hour, (c) heart rate, (d) respiration rate, and (e) physical activity for the same patient shown in Fig. 5a, c-g, with the intensity or amplitude information of the associated events color-coded in each time bin. (f) The time series plot of coughing counts organized in days post the test-positive date from eights COVID-19 patients. (g) The age distribution of the 27 patients whose data are not used to build the machine learning model. (h) The histogram of coughing frequency of the 27 patients. (i) The cough intensity versus cough frequency analyzed for each hour of data, clustered by four demographic groups.

Supplemental Information
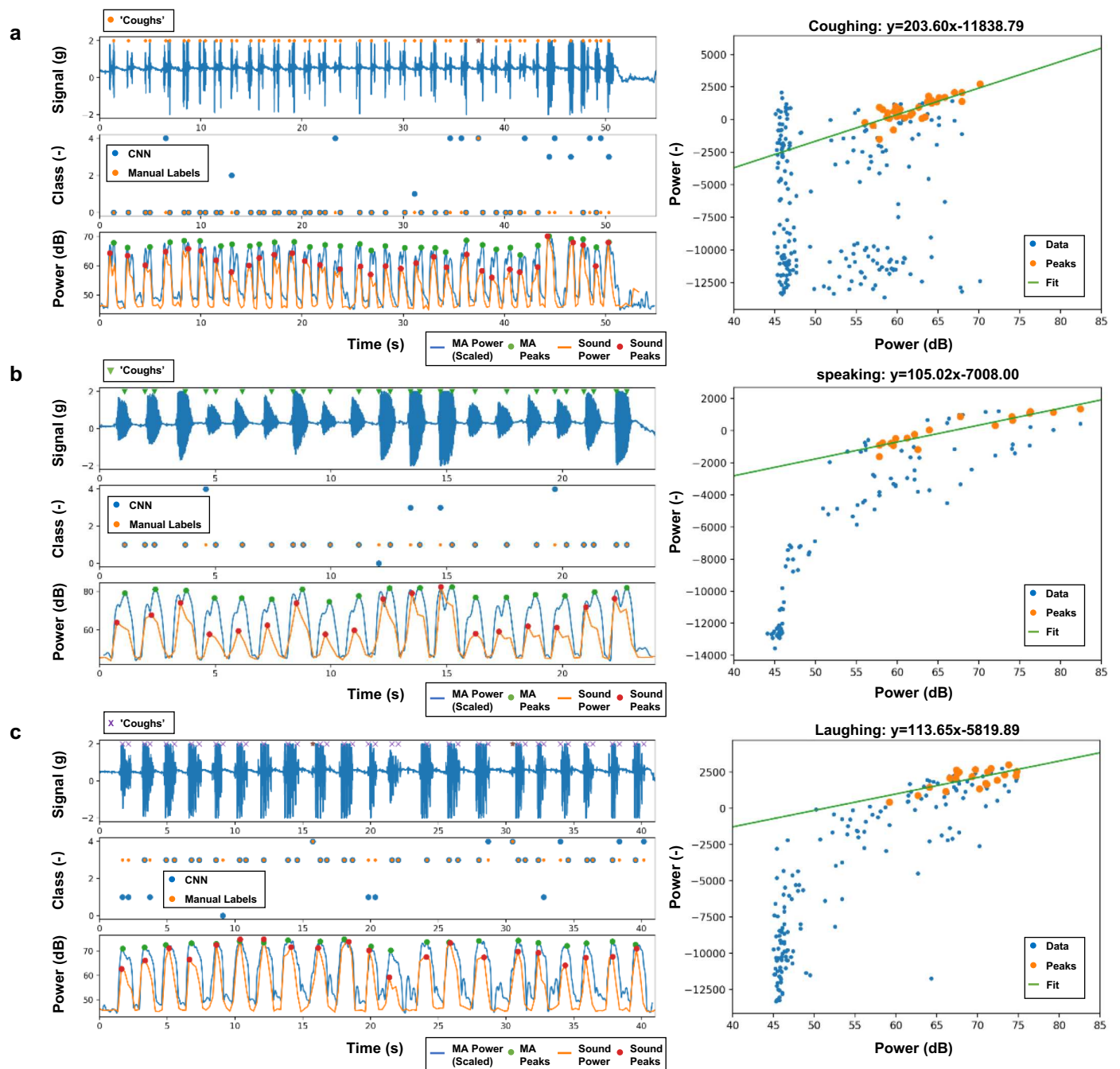
Fig. S1. Mechano-acoustic measurement of vocal event intensity. The time series of MA measurement, CNN-classification of the detected cough-like events in comparison with the manual labeling, and the scaled MA power synced with the decibel meter measurement of sound power for (a) coughing, (b) speaking, and (c) Laughing. Figures on the right show the correlation between MA power and sound power.
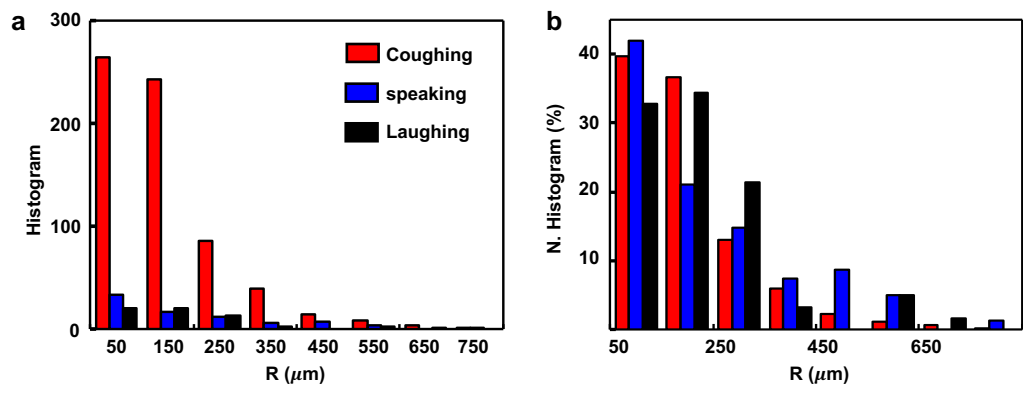
Fig. S2. Histogram of droplet sizes for coughing, speaking and laughing events. (a) Unnormalized and (b) Normalized histograms.
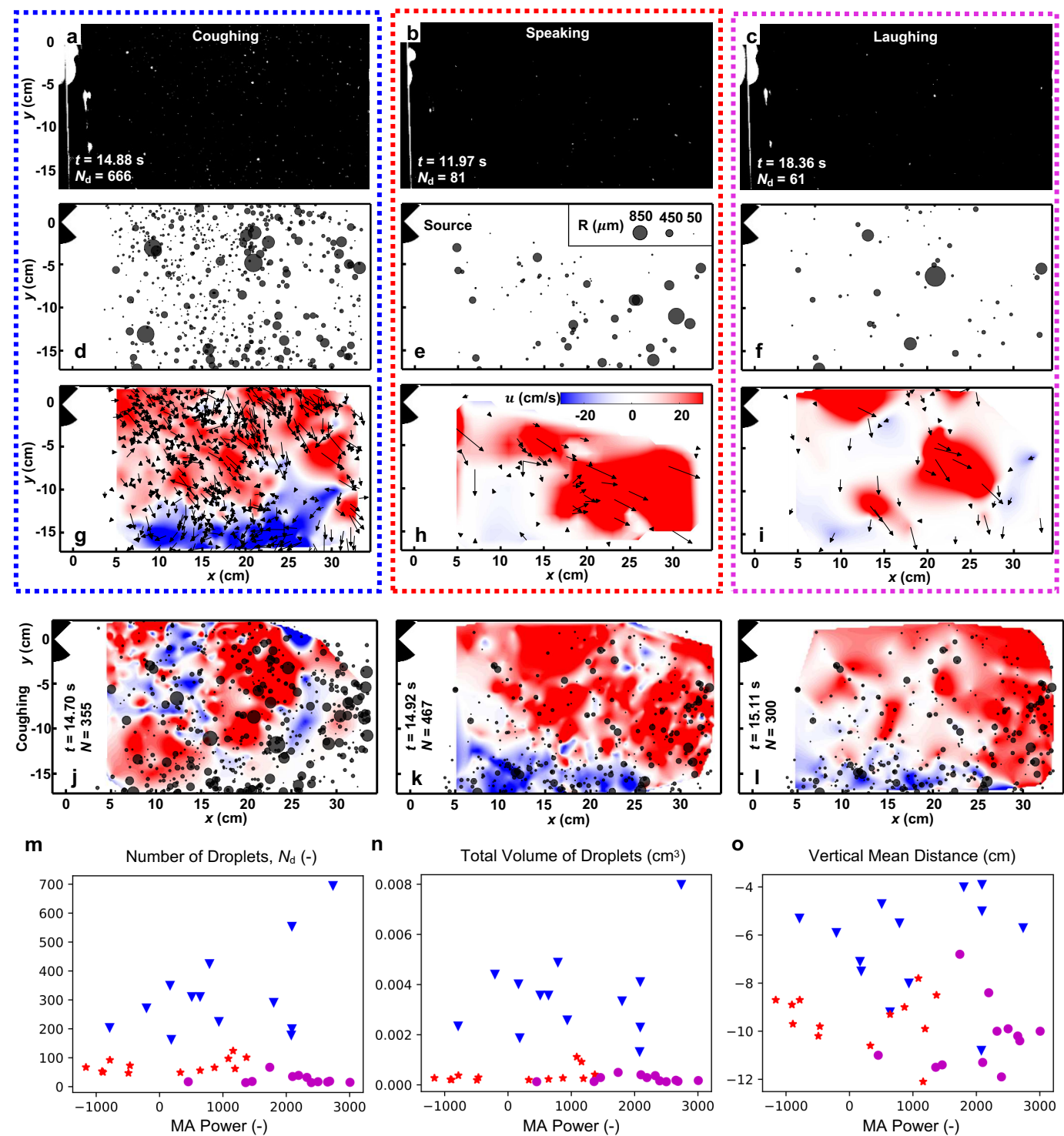
Fig. S3. Additional data on droplet dynamics. (a,b,c) Images of coughing, speaking, and laughing events at representative instants. (d,e,f) Detected droplets with sizes indicated by the diameters of the grey circular symbols (g,h,i) velocity vector and contour fields at the times corresponding to those in (a,b,c); the color denotes streamwise velocity. (j,k,l) Sequence of coughing at t=14.70s,14.92s,15.11s. (m,n,o) The total number, total volume, and vertical mean distance of produced droplets vs. MA power for coughing (blue), speaking (red), and laughing (magenta).
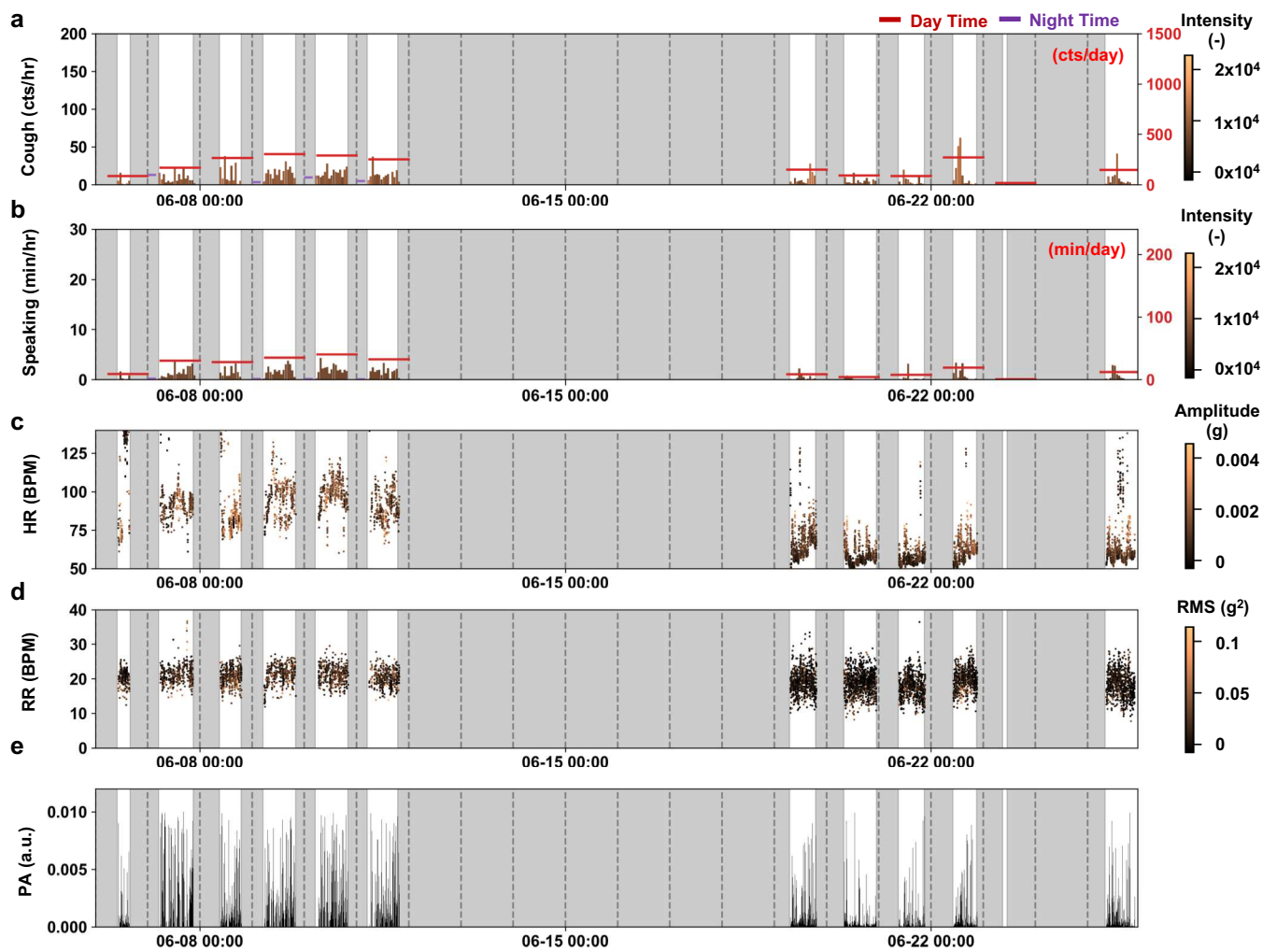
Fig. S4. Long-term monitoring of respiratory biomarkers and vital signs. Results for (a) coughing, (b) speaking, (c) heart rate, (d) respiration rate, and (e) physical activity of COVID-19 patient # SRALRN5F.
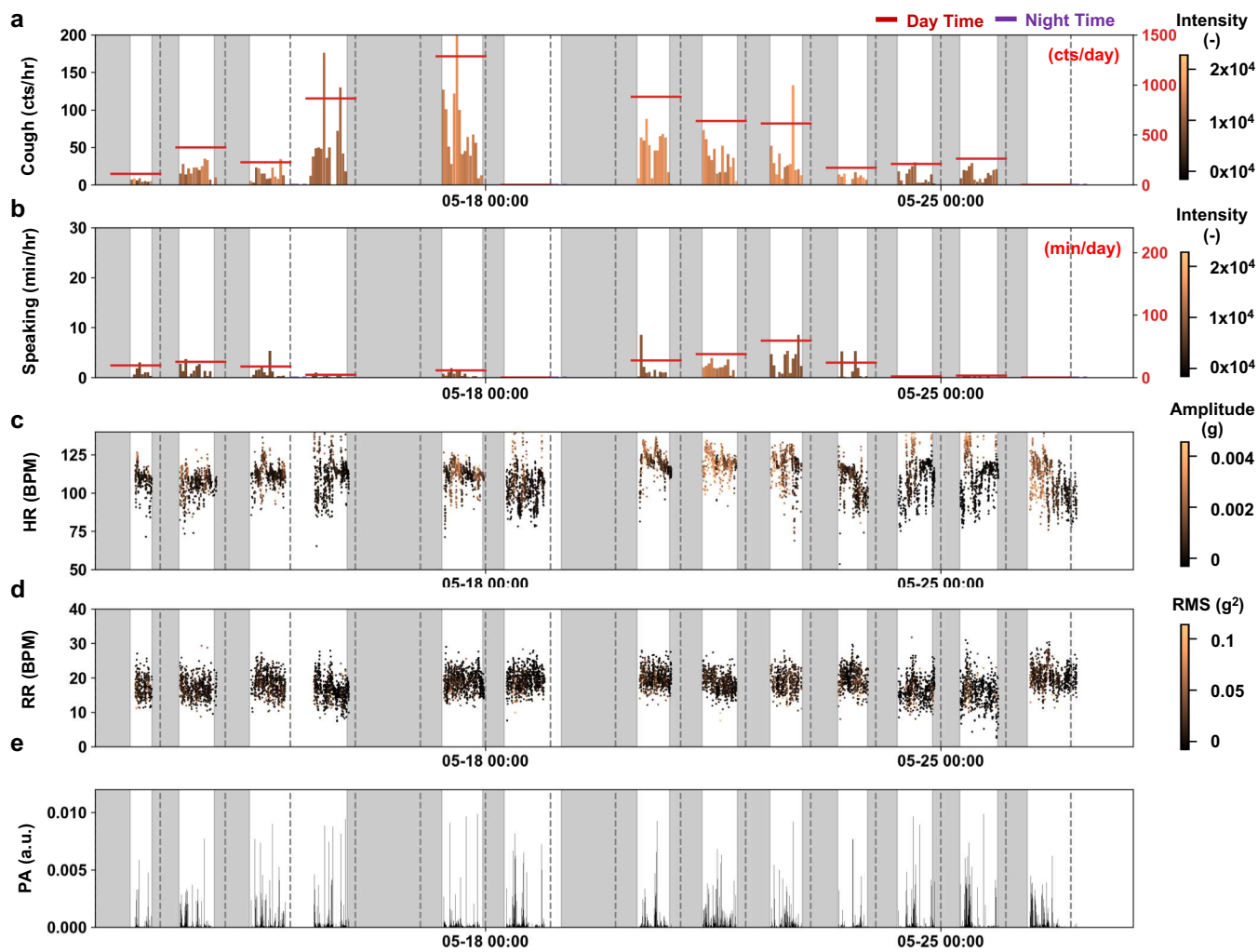
Fig. S5. Long-term monitoring of respiratory biomarkers and vital signs. Results for (a) coughing, (b) speaking, (c) heart rate, (d) respiration rate, and (e) physical activity of COVID-19 patient # SRAL2014F.
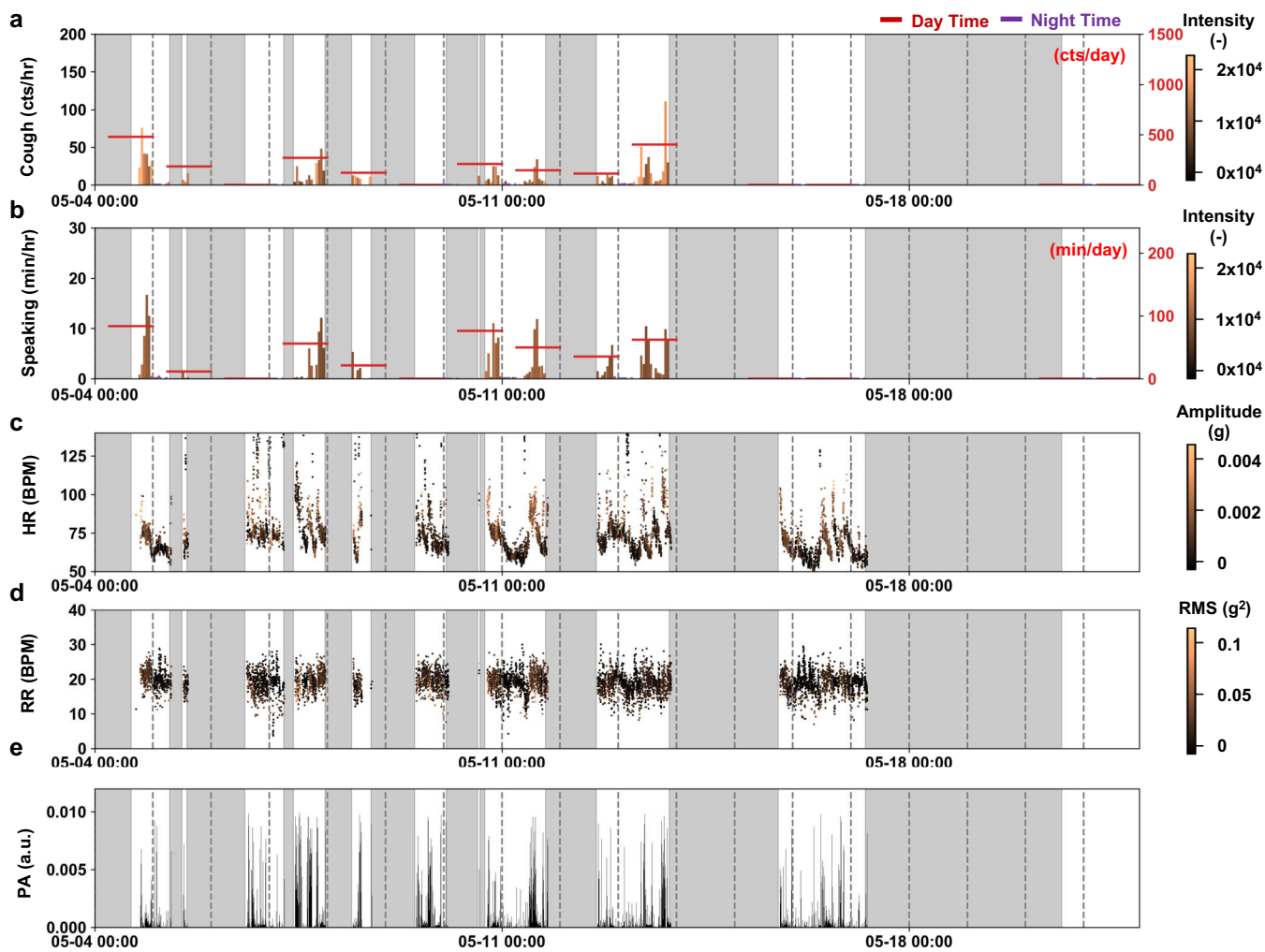
Fig. S6. Long-term monitoring of respiratory biomarkers and vital signs. Results for (a) coughing, (b) speaking, (c) heart rate, (d) respiration rate, and (e) physical activity of COVID-19 patient # SRALH11F.

Fig. S7. Long-term monitoring of respiratory biomarkers and vital signs. Results for (a) coughing, (b) speaking, (c) heart rate, (d) respiration rate, and (e) physical activity of COVID-19 patient # SRAL2024M.

Fig. S8. Long-term monitoring of respiratory biomarkers and vital signs. Results for (a) coughing, (b) speaking, (c) heart rate, (d) respiration rate, and (e) physical activity of COVID-19 patient # SRAL-M-H2.

Fig. S9. Long-term monitoring of respiratory biomarkers and vital signs. Results for (a) coughing, (b) speaking, (c) heart rate, (d) respiration rate, and (e) physical activity of COVID-19 patient # SRAL2012BM.

Fig. S10. Long-term monitoring of respiratory biomarkers and vital signs. Results for (a) coughing, (b) speaking, (c) heart rate, (d) respiration rate, and (e) physical activity of COVID-19 patient # SRAL2021F.
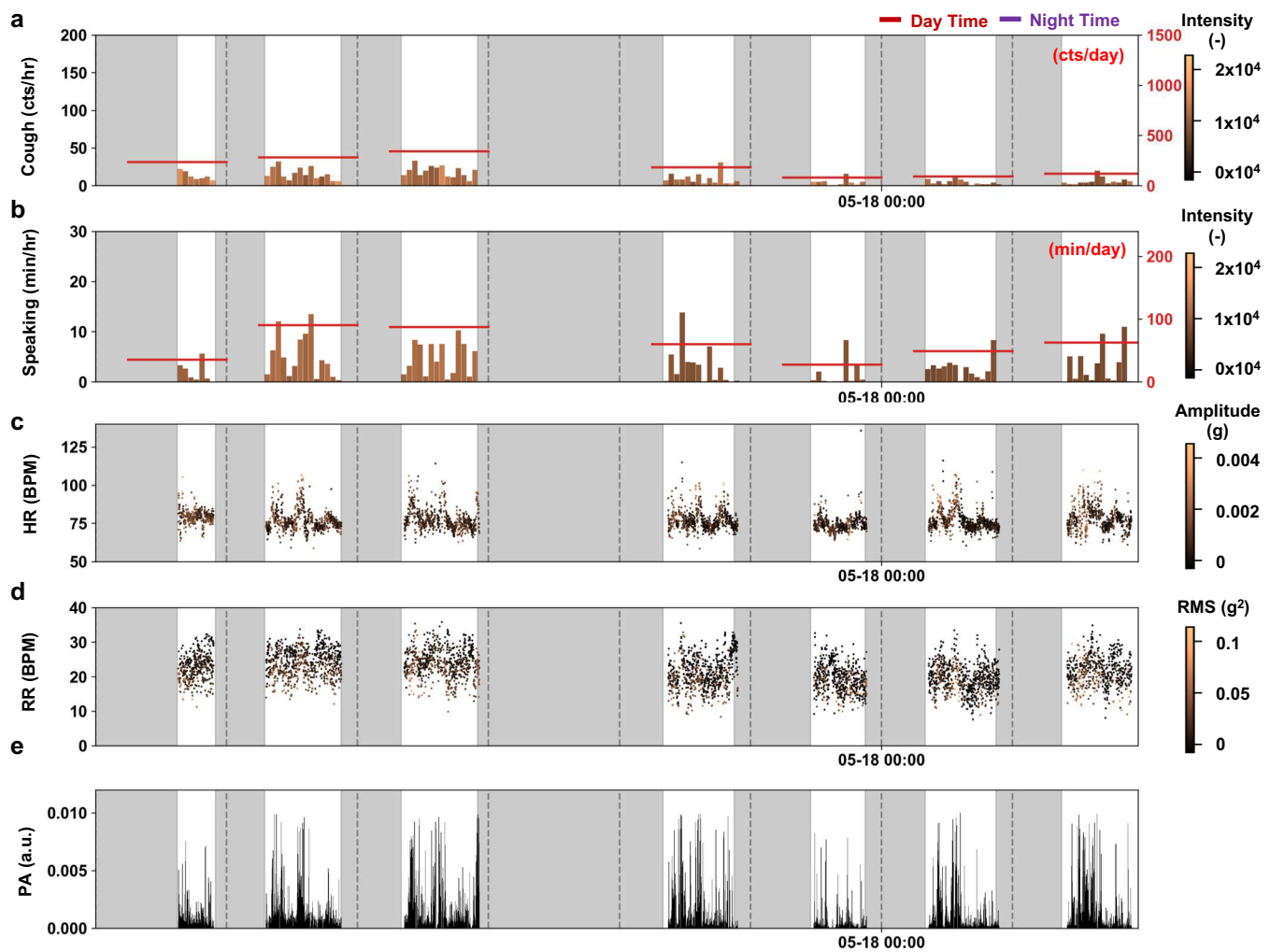
Fig. S11. Long-term monitoring of respiratory biomarkers and vital signs. Results for (a) coughing, (b) speaking, (c) heart rate, (d) respiration rate, and (e) physical activity of COVID-19 patient # SRAL2032F.

Fig. S12. Long-term monitoring of respiratory biomarkers and vital signs. Results for (a) coughing, (b) speaking, (c) heart rate, (d) respiration rate, and (e) physical activity of COVID-19 patient # SRAL7-M-MGR.

Fig. S13. Long-term monitoring of respiratory biomarkers and vital signs. Results for (a) coughing, (b) speaking, (c) heart rate, (d) respiration rate, and (e) physical activity of COVID-19 patient # SRAL1921F.
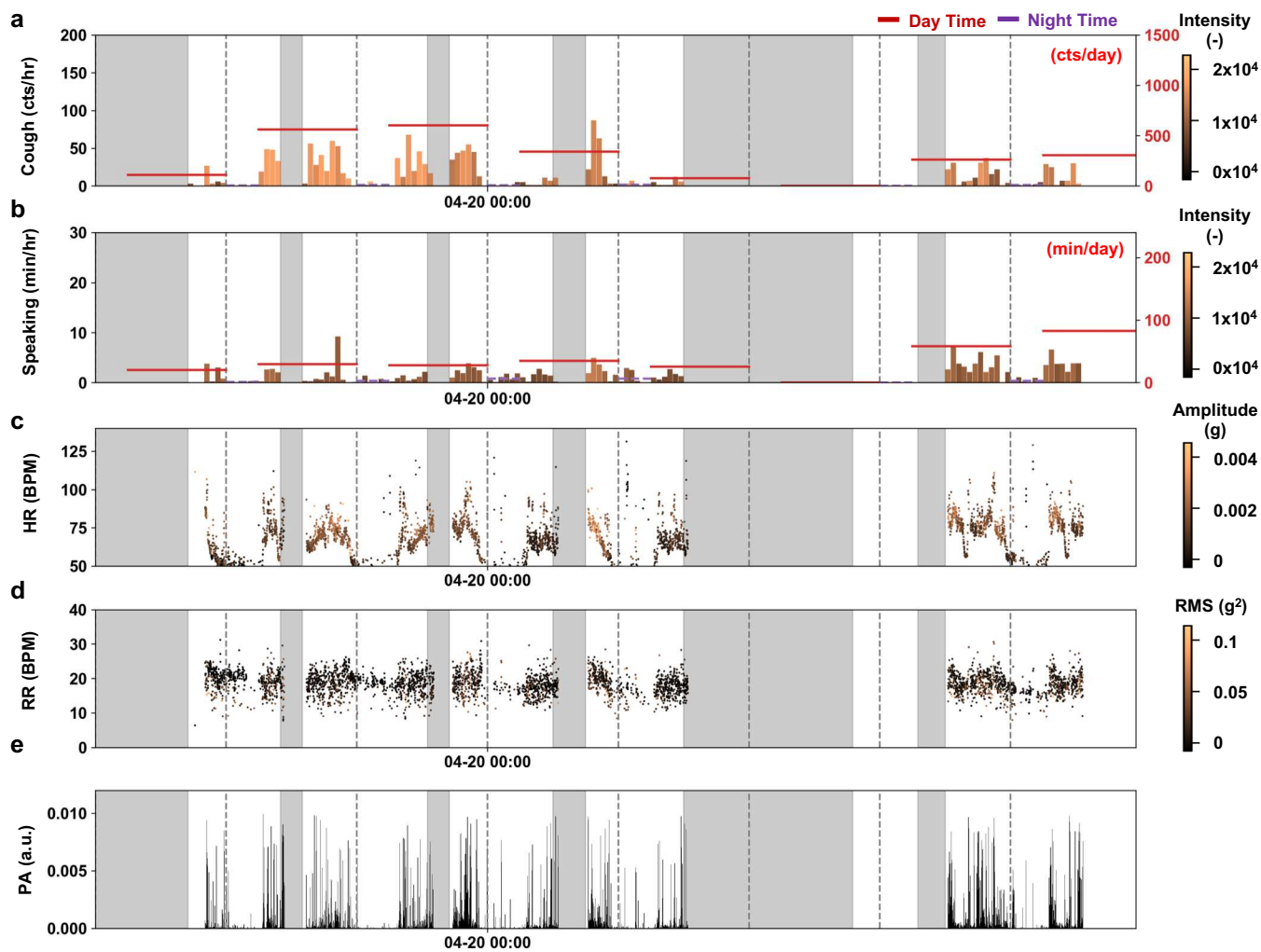
Fig. S14. Long-term monitoring of respiratory biomarkers and vital signs. Results for (a) coughing, (b) speaking, (c) heart rate, (d) respiration rate, and (e) physical activity of COVID-19 patient # SRAL2031M.
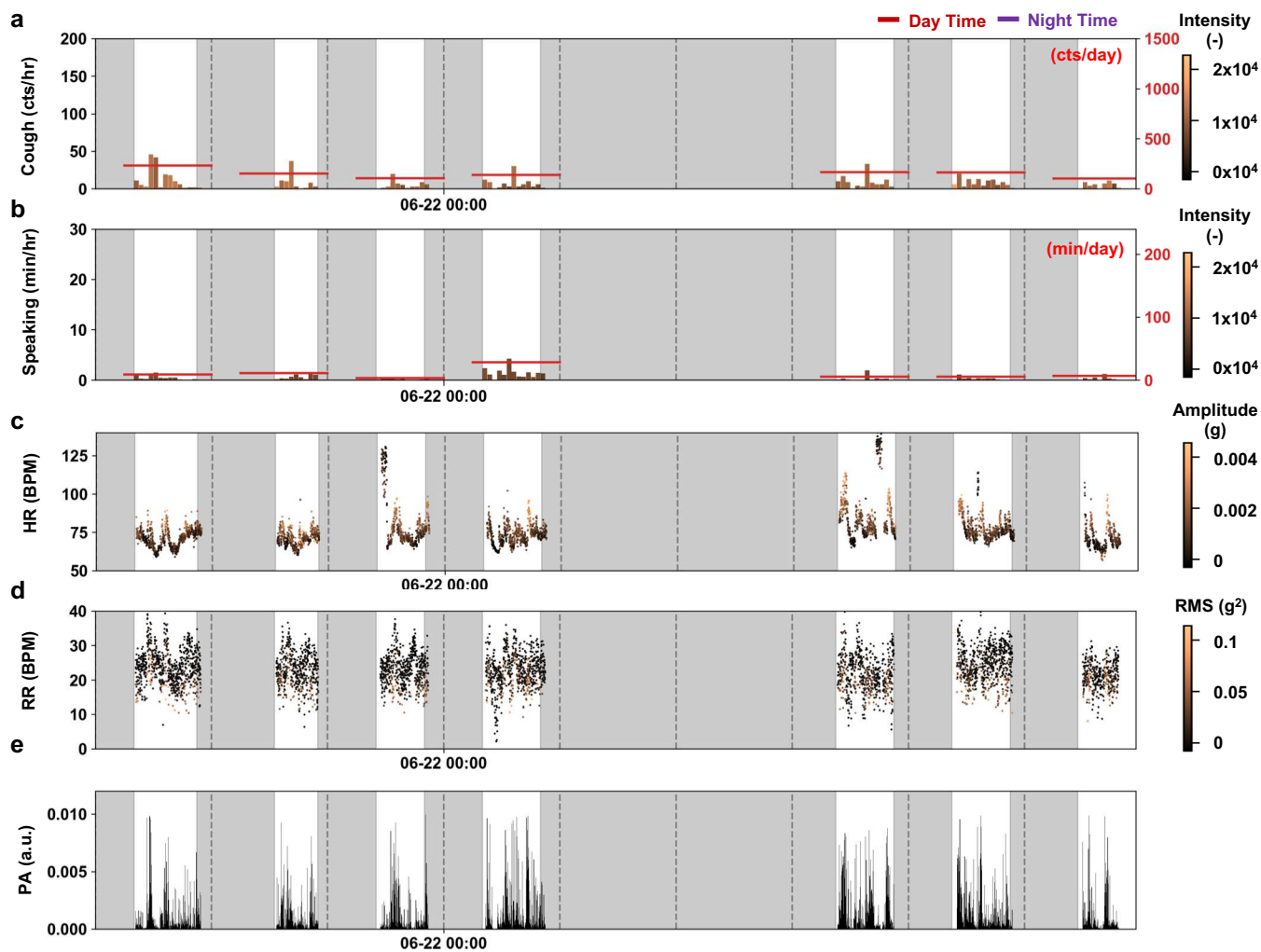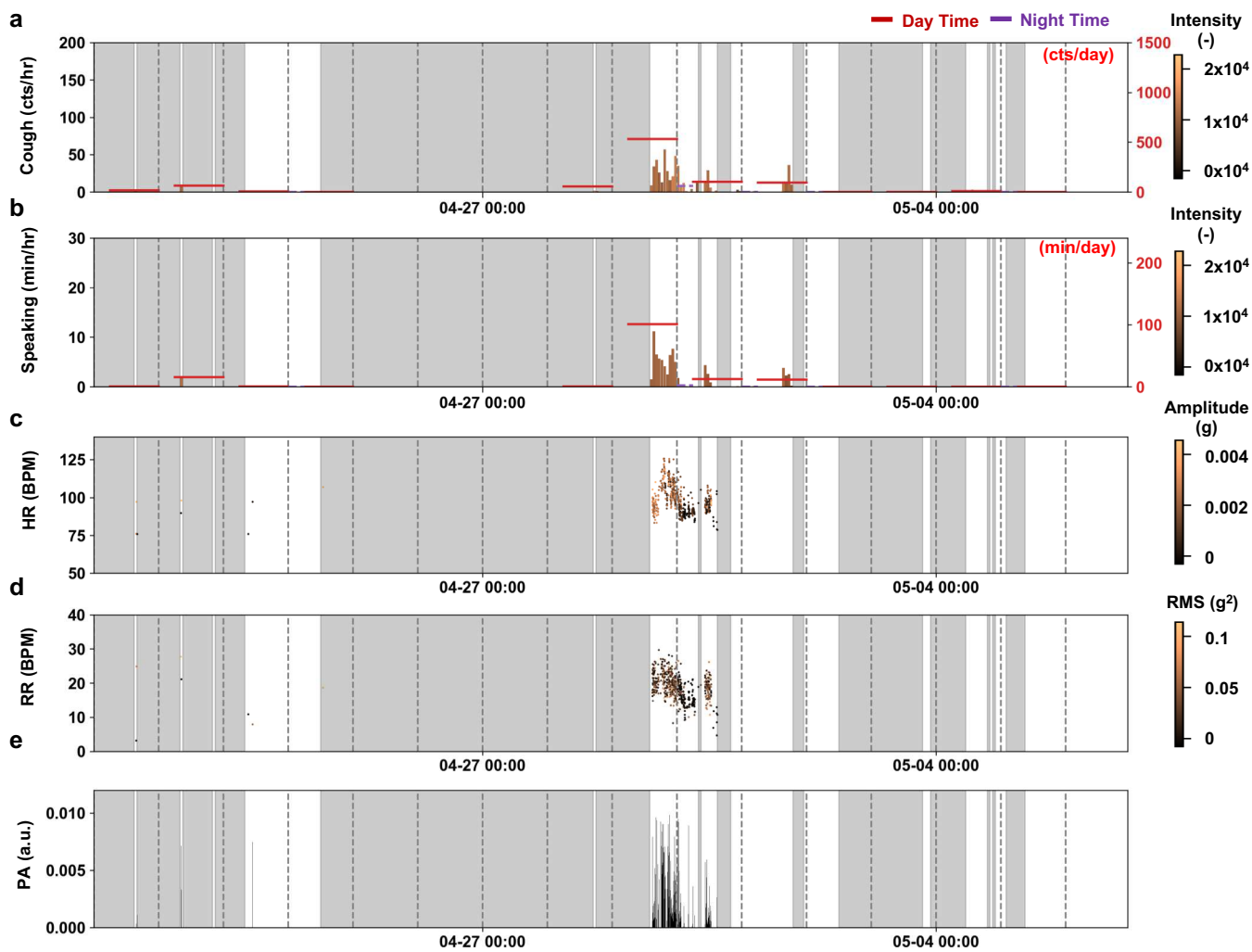
Fig. S15. Long-term monitoring of respiratory biomarkers and vital signs. Results for (a) coughing, (b) speaking, (c) heart rate, (d) respiration rate, and (e) physical activity of COVID-19 patient # NM12F.
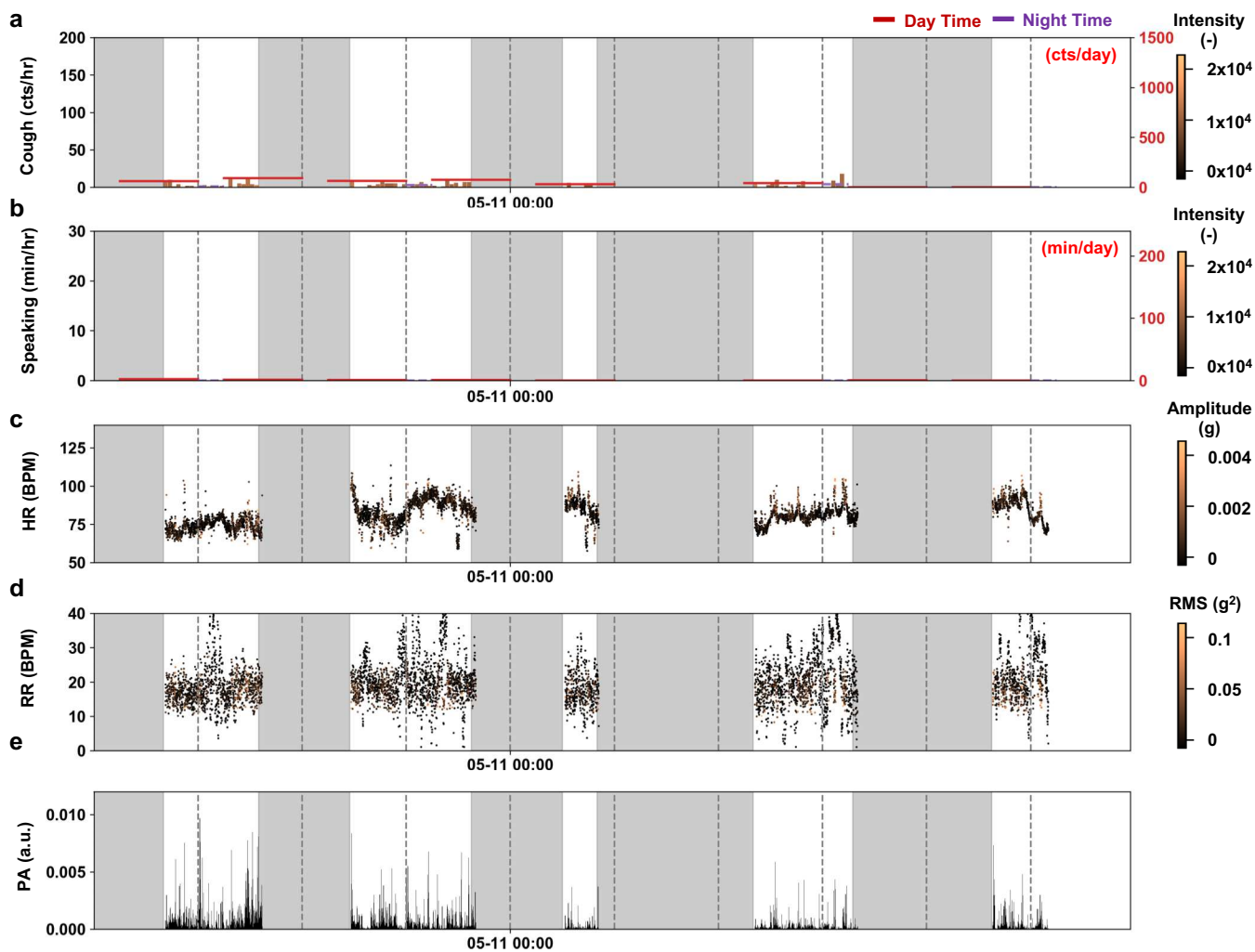
Fig. S16. Long-term monitoring of respiratory biomarkers and vital signs. Results for (a) coughing, (b) speaking, (c) heart rate, (d) respiration rate, and (e) physical activity of COVID-19 patient # NM17m.
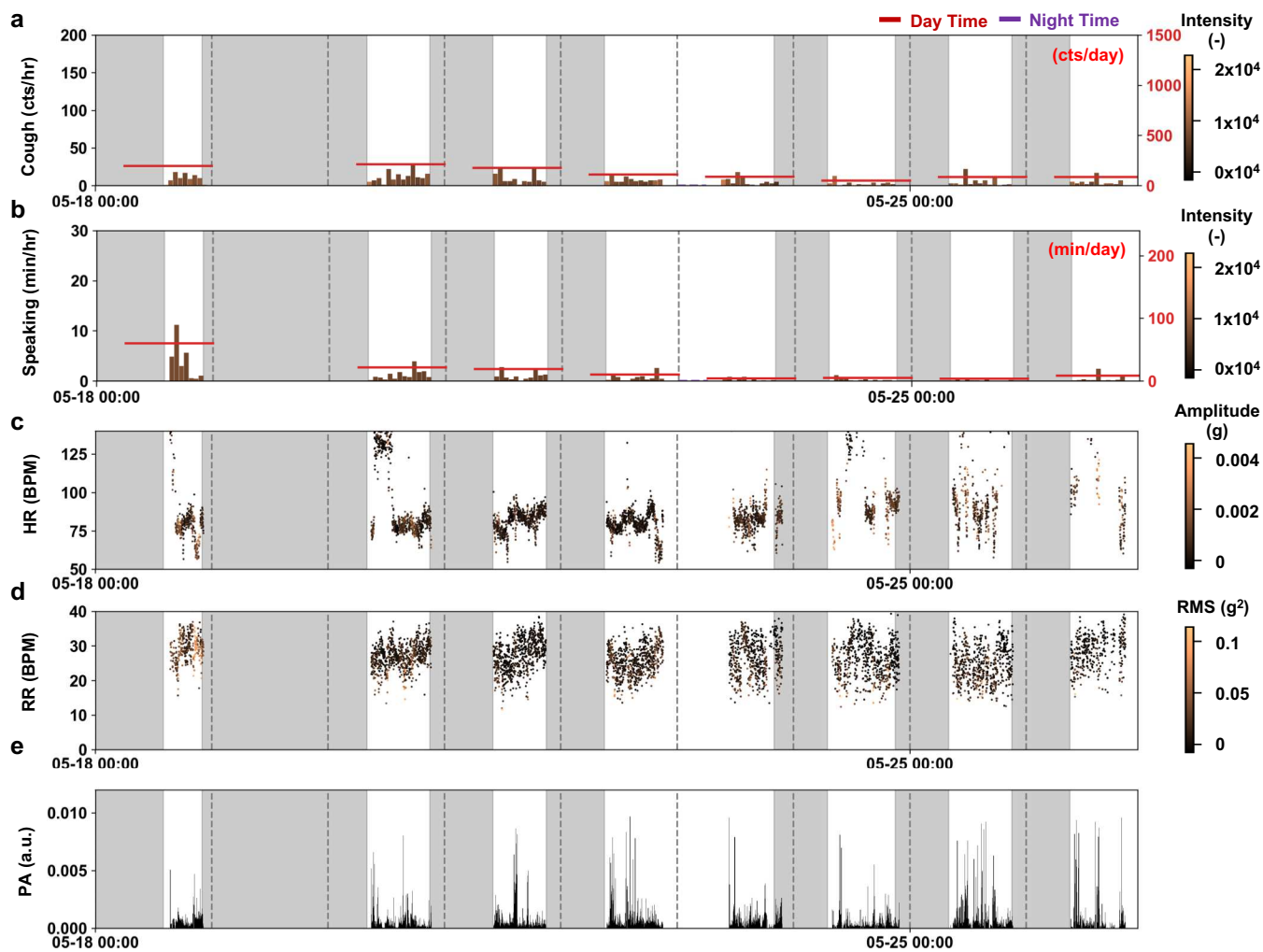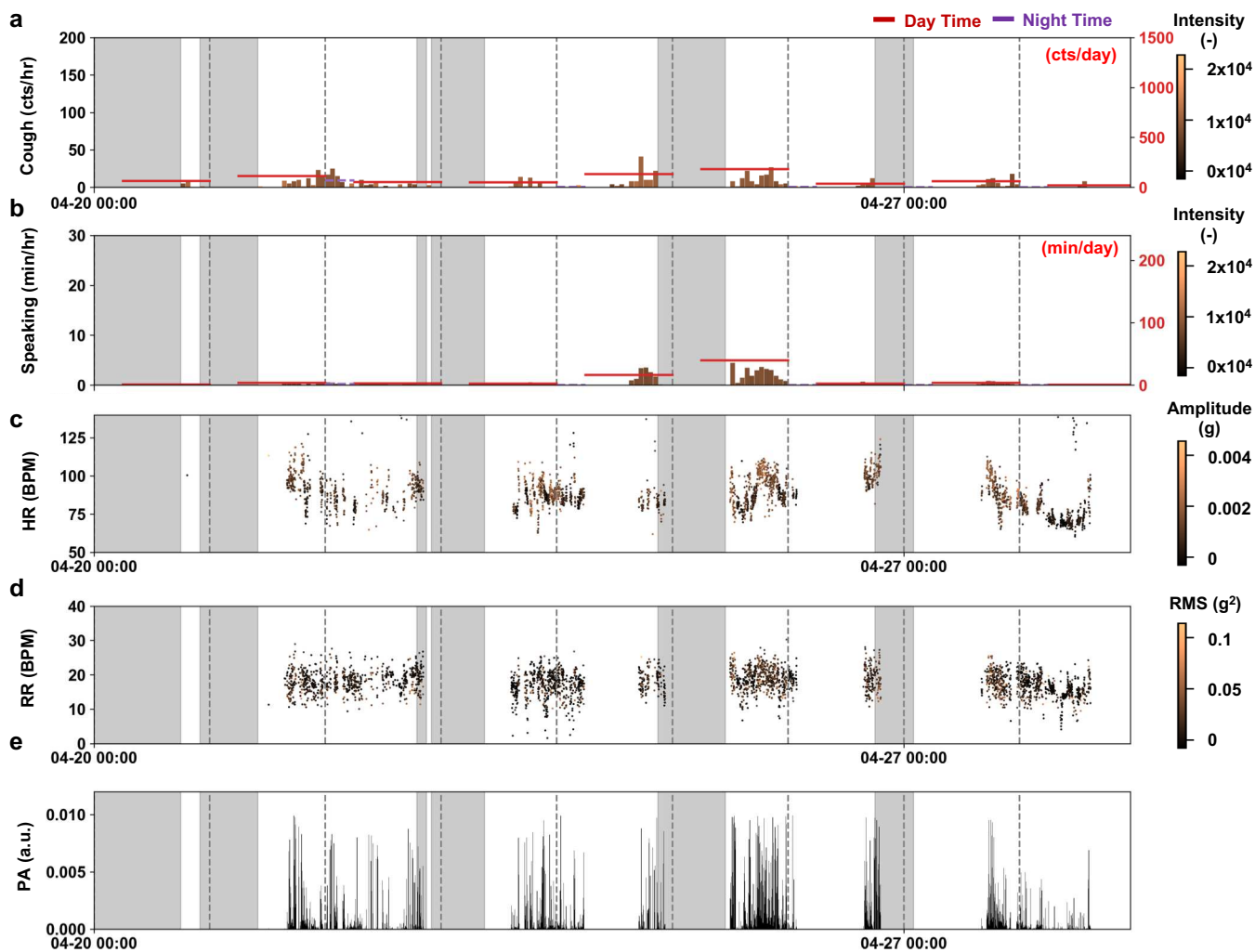
Fig. S17. Long-term monitoring of respiratory biomarkers and vital signs. Results for (a) coughing, (b) speaking, (c) heart rate, (d) respiration rate, and (e) physical activity of COVID-19 patient # SRAL-F-H5.
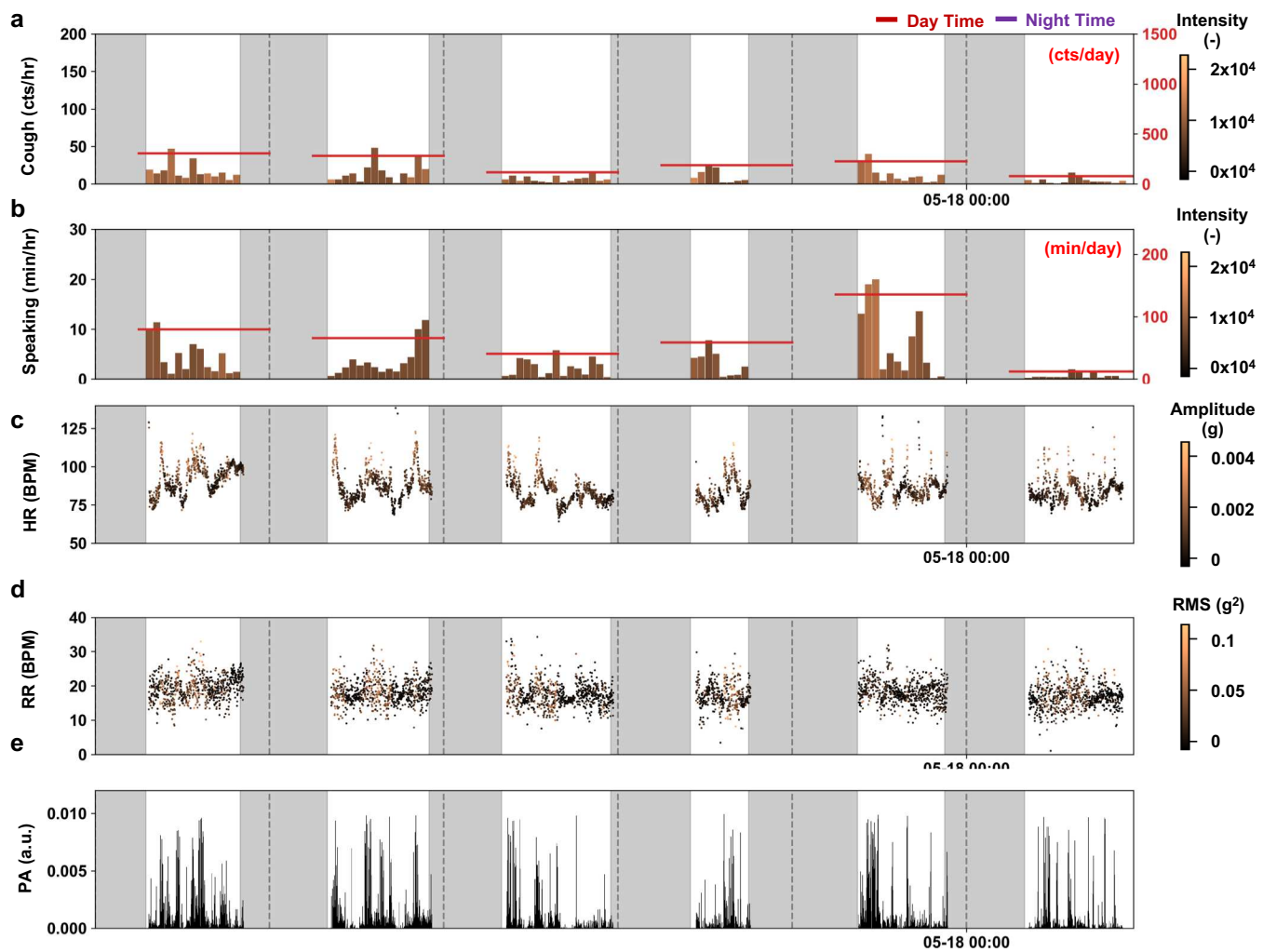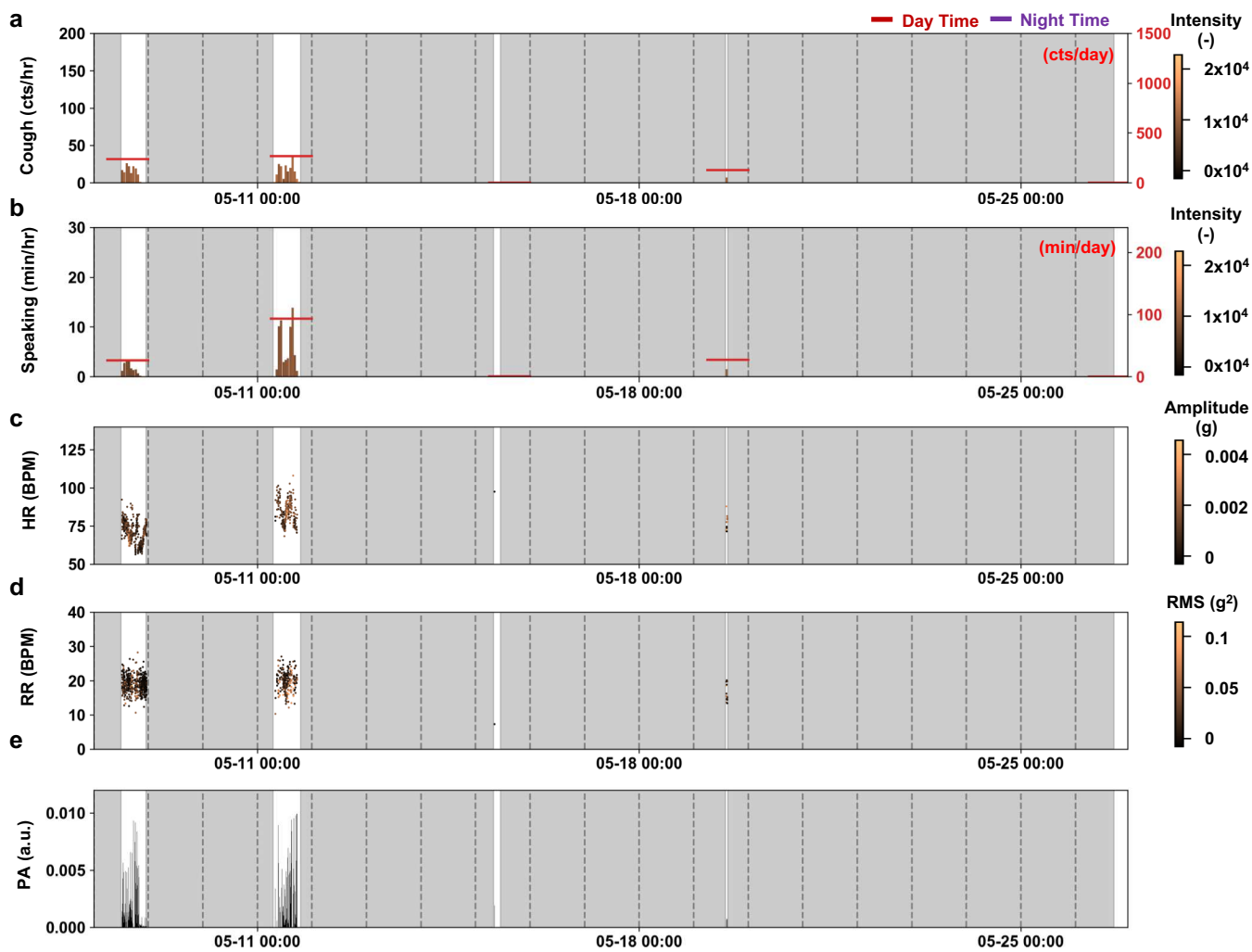
Fig. S18. Long-term monitoring of respiratory biomarkers and vital signs. Results for (a) coughing, (b) speaking, (c) heart rate, (d) respiration rate, and (e) physical activity of COVID-19 patient # SRALPT1F.
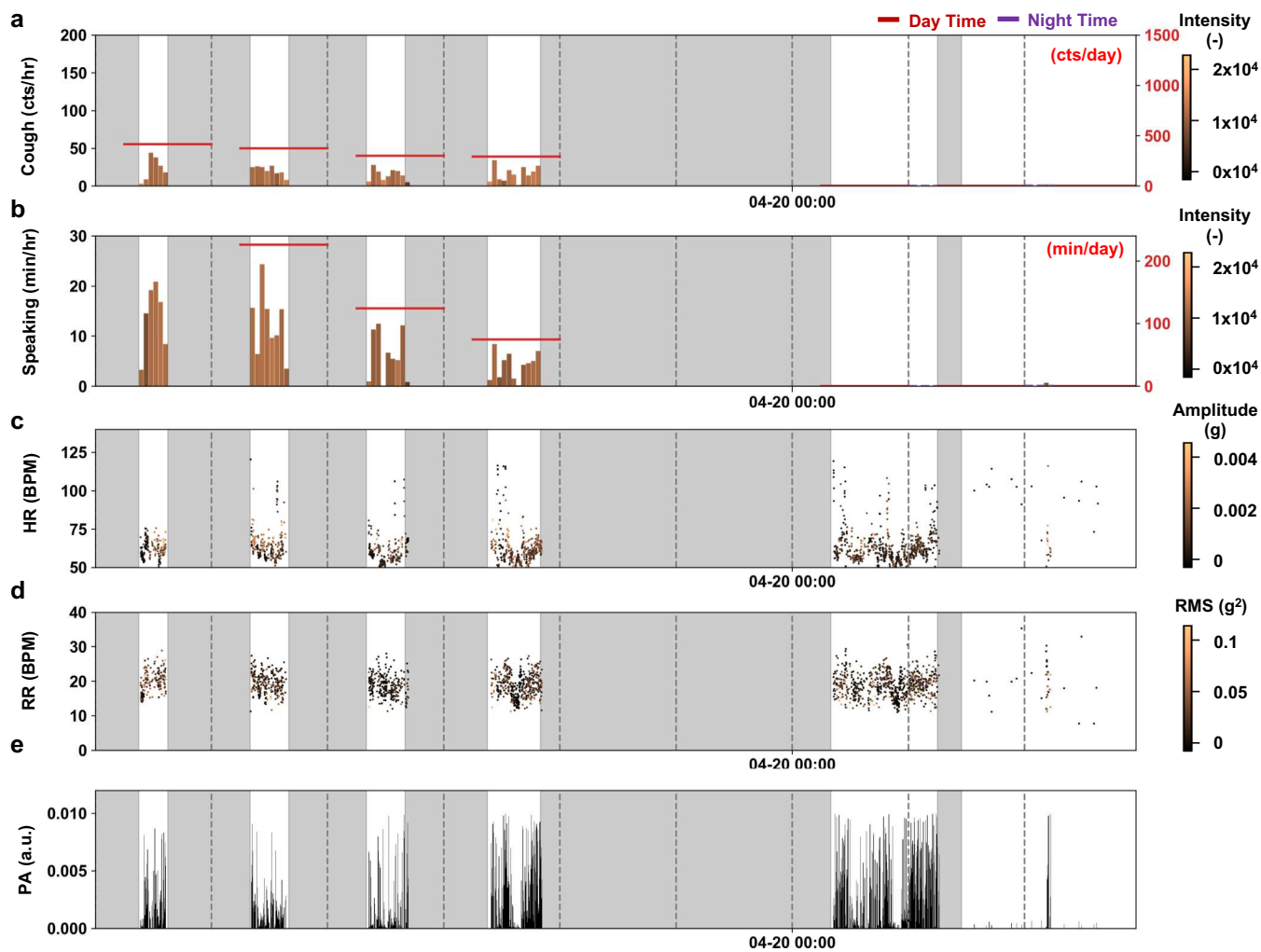
Fig. S19. Long-term monitoring of respiratory biomarkers and vital signs. Results for (a) coughing, (b) speaking, (c) heart rate, (d) respiration rate, and (e) physical activity of COVID-19 patient # SRAL1923M.
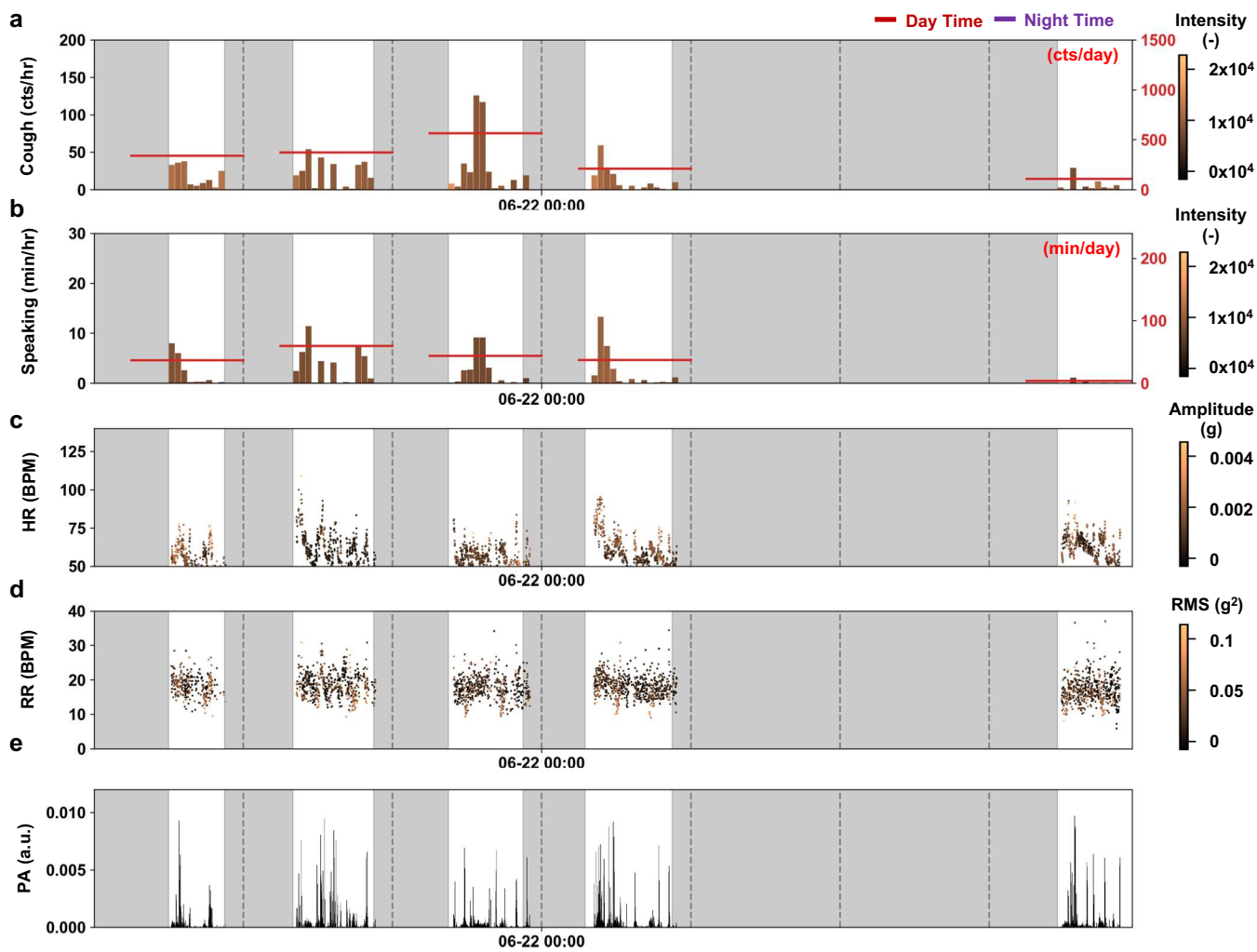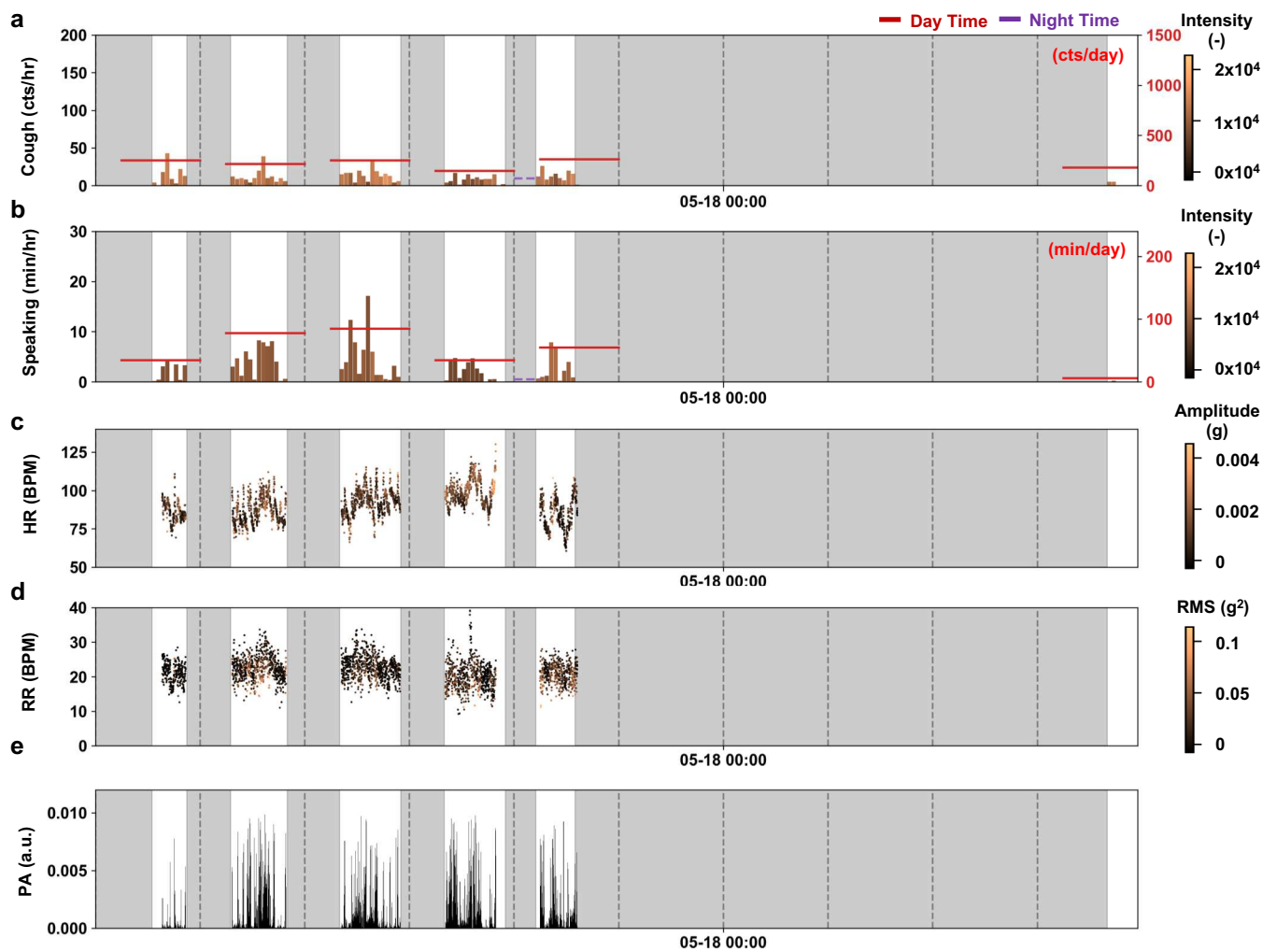
Fig. S20. Long-term monitoring of respiratory biomarkers and vital signs. Results for (a) coughing, (b) speaking, (c) heart rate, (d) respiration rate, and (e) physical activity of COVID-19 patient # SRALH8M.
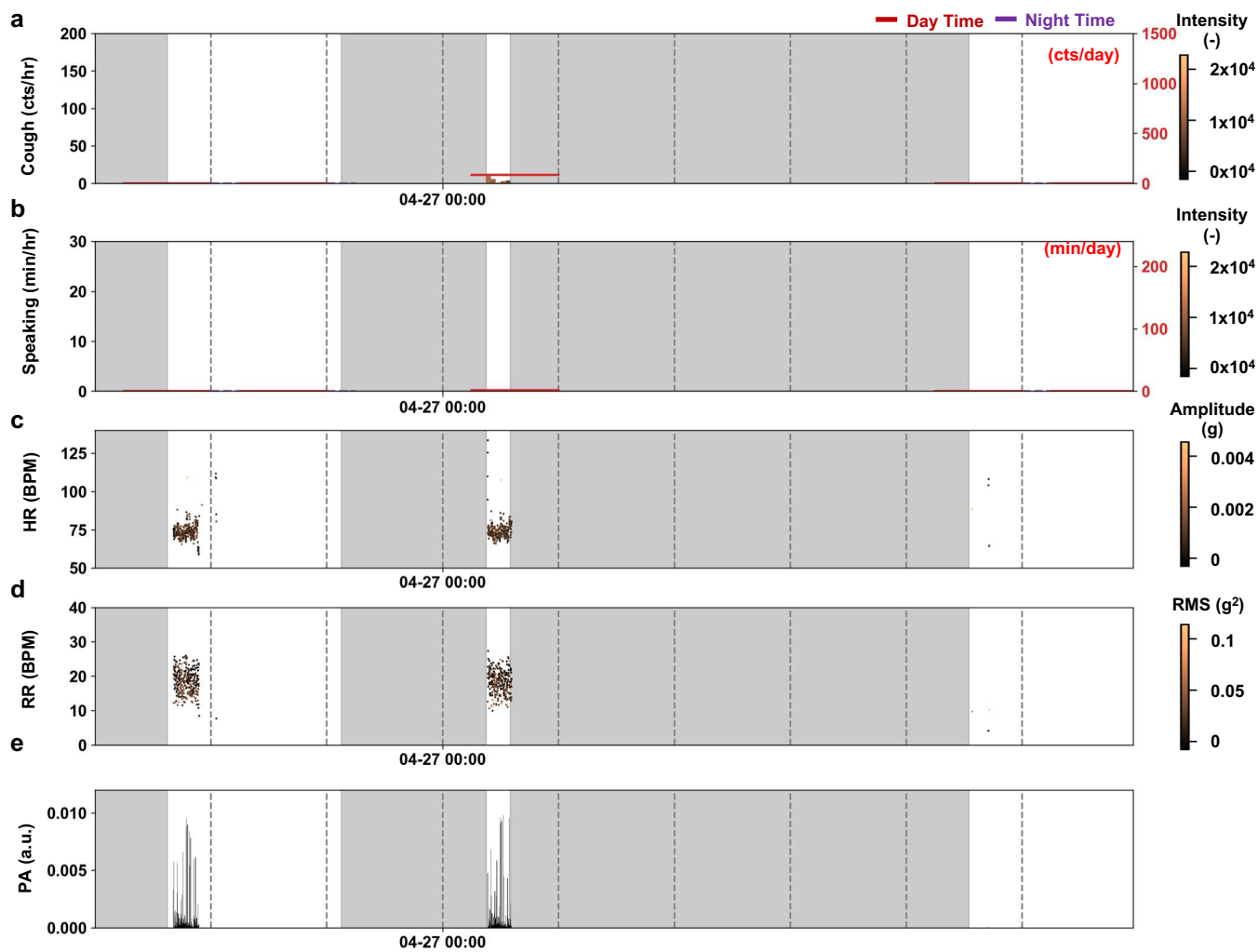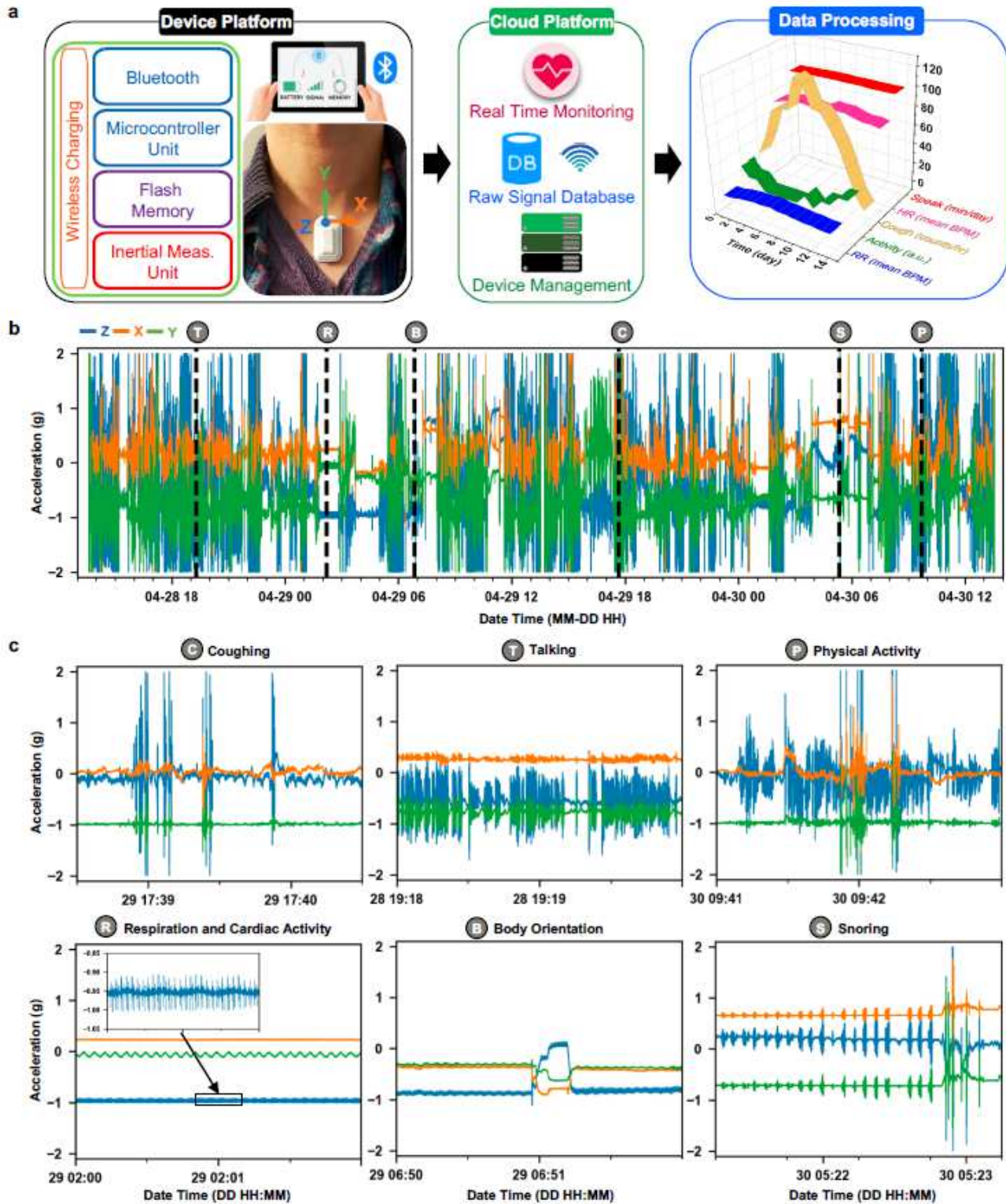
Usage	#	ID	Gender	Age	Status	Start Date	Days of Enrollment	Hours of recording	PCR+ Date
Testing	1	SRAL-F-H5	F	25	Patient	20-04-20	8	143	NR
Testing	2	SRALPT1F	F	30	Patient	20-05-08	19	29	NR
Testing	3	NM12F	F	45	Patient	20-04-21	15	114	20-04-18
Testing	4	SRALH11F	F	52	Patient	20-05-04	17	182	20-04-09
Testing	5	SRALDOC3F	F	52	Patient	20-04-23	5	16	NR
Testing	6	NM15F	F	53	Patient	20-04-24	31	135	20-04-03
Testing	7	SRAL2032F	F	59	Patient	20-05-13	7	77	NR
Testing	8	SRAL2030F	F	65	Patient	20-05-12	3	35	NR
Testing	9	SRAL2014F	F	65	Patient	20-05-12	15	188	20-05-03
Testing	10	SRAL2023F	F	66	Patient	20-05-20	3	42	NR
Testing	11	SRAL2022F	F	69	Patient	20-05-13	6	56	NR
Testing	12	SRAL2021F	F	72	Patient	20-05-18	9	107	NR
Testing	13	SRALRN3F	F	NR	Patient	20-05-08	6	92	NR
Testing	14	SRAL1921F	F	NR	Patient	20-06-19	7	58	NR
Testing	15	SRALRN5F	F	NR	Patient	20-06-06	20	142	NR
Testing	16	SRAL2033M	M	32	Patient	20-05-22	6	59	NR
Testing	17	SRAL-M-H2	M	34	Patient	20-04-17	7	113	20-04-11
Testing	18	SRAL7-M-MGR	M	41	Patient	20-04-14	8	88	NR
Testing	19	SRALH8M	M	45	Patient	20-04-24	8	74	NR
Testing	20	SRAL2015M	M	52	Patient	20-05-12	4	44	NR
Testing	21	SRAL2024BM	M	55	Patient	20-05-27	6	51	NR
Testing	22	SRAL2012BM	M	55	Patient	20-06-19	9	77	NR
Testing	23	NM17M	M	56	Patient	20-05-07	9	114	20-05-05
Testing	24	SRAL2024M	M	60	Patient	20-05-12	8	83	20-03-28
Testing	25	SRAL2031M	M	61	Patient	20-05-12	10	60	20-04-21
Testing	26	SRAL1922M	M	NR	Patient	20-06-19	1	6	NR
Testing	27	SRAL1923M	M	NR	Patient	20-06-19	25	31	NR
Training	1	NU-M-1	M	37	Healthy	20-05-09	1	5	NA
Training	2	NU-M-2	M	53	Healthy	20-05-02	1	5	NA
Training	3	NU-M-3	M	29	Healthy	20-05-09	1	6	NA
Training	4	NU-F-1	F	26	Healthy	20-05-13	1	8	NA
Training	5	NU-M-4	M	30	Healthy	20-05-11	1	24	NA
Training	6	NU-F-2	F	29	Healthy	20-05-13	1	23	NA
Training	7	NU-F-3	F	29	Healthy	20-05-15	1	22	NA
Training	8	NU-M-5	M	40	Healthy	20-05-15	1	18	NA
Training	9	NU-F-4	F	27	Healthy	20-05-16	2	19	NA
Training	10	NU-M-6	M	25	Healthy	20-06-10	1	2	NA
Training	11	SRAL-F-H1	F	31	Patient	20-04-17	10	115	NR
Training	12	SRAL-F-H4	F	21	Patient	20-04-21	9	142	NR
Training	13	SRAL-F-H6	F	48	Patient	20-04-21	9	113	NR
Training	14	SRAL-M-H3	M	59	Patient	20-04-17	13	171	NR
Training	15	SRAL2020BF	F	64	Patient	20-05-29	13	38	NR
Training	16	SRAL2025M	M	75	Patient	20-05-19	8	101	NR
Training	17	SRAL2026F	F	68	Patient	20-05-21	4	58	NR
Training	18	SRAL2032BM	M	52	Patient	20-05-29	7	60	NR
Training	19	SRAL2019M	M	60	Patient	20-06-05	10	38	NR
Training	20	SRAL2006M	M	59	Patient	20-06-19	8	59	NR
Note:									
	NR = Not Reported								
	NA=Not Applicable								

Tab. S1. Demographic information for all the participants in the study.

Usage	#	ID	Cough				Speak				Throat clearing				Laugh				Motion artifact			
			Labeled # of events	sens.	spec.	prec.	Labeled # of events	sens.	spec.	prec.	Labeled # of events	sens.	spec.	prec.	Labeled # of events	sens.	spec.	prec.	Labeled # of events	sens.	spec.	prec.
Testing	1	SRAL-F-H5																				
Testing	2	SRALPT1F																				
Testing	3	NM12F																				
Testing	4	SRALH11F	185	0.98	0.86	0.71	182	0.64	1.00	1.00	62	0.92	0.97	0.74	95	0.54	0.97	0.73	183	0.97	0.98	0.94
Testing	5	SRALDOC3F																				
Testing	6	NM15F	292	0.97	0.98	0.95	291	0.96	1.00	1.00	51	0.98	1.00	1.00	51	0.80	0.99	0.84	291	1.00	0.99	0.97
Testing	7	SRAL2032F	384	0.76	0.96	0.88	381	0.47	0.98	0.90	119	0.89	0.89	0.43	145	0.84	0.91	0.50	382	0.88	0.95	0.86
Testing	8	SRAL2030F																				
Testing	9	SRAL2014F	406	0.78	0.98	0.95	404	0.74	0.98	0.96	62	0.94	0.94	0.44	13	0.92	0.94	0.14	404	0.91	0.94	0.87
Testing	10	SRAL2023F																				
Testing	11	SRAL2022F																				
Testing	12	SRAL2021F	410	0.69	0.98	0.93	407	0.78	0.99	0.96	184	0.97	0.90	0.59	11	0.73	1.00	0.57	408	1.00	0.94	0.86
Testing	13	SRALRN3F																				
Testing	14	SRAL1921F	232	1.00	0.95	0.87	229	0.93	1.00	1.00	99	1.00	1.00	1.00	117	0.69	0.98	0.86	232	1.00	0.99	0.98
Testing	15	SRALRN5F																				
Testing	16	SRAL2033M																				
Testing	17	SRAL-M-H2	301	0.99	1.00	0.99	298	0.97	1.00	1.00	101	0.98	1.00	0.99	86	0.99	0.99	0.86	300	0.99	1.00	1.00
Testing	18	SRAL7-M-MGR	180	0.71	0.89	0.62	177	0.47	0.89	0.52	179	0.55	0.92	0.64	178	0.51	0.92	0.62	177	0.75	0.87	0.59
Testing	19	SRALH8M																				
Testing	20	SRAL2015M																				
Testing	21	SRAL2024BM																				
Testing	22	SRAL2012BM	287	0.94	0.97	0.92	284	0.64	0.98	0.93	249	0.90	0.94	0.82	12	0.92	0.96	0.19	285	0.93	0.96	0.90
Testing	23	NM17M																				
Testing	24	SRAL2024M	108	0.86	0.88	0.69	105	0.50	0.99	0.91	106	0.77	0.91	0.73	27	0.93	0.94	0.51	106	0.88	0.99	0.95
Testing	25	SRAL2031M																				
Testing	26	SRAL1922M																				
Testing	27	SRAL1923M																				
Training	1	NU-M-1	126	1.00	0.99	0.97	221	0.98	0.99	0.97	124	0.88	0.99	0.96	146	0.99	0.99	0.95	157	0.99	1.00	1.00
Training	2	NU-M-2	184	0.96	0.98	0.90	123	0.97	0.96	0.77	179	0.74	0.99	0.96	206	0.88	0.98	0.91	304	1.00	0.99	0.98
Training	3	NU-M-3	143	1.00	0.99	0.92	291	0.89	0.96	0.90	133	0.92	0.98	0.87	177	0.82	0.99	0.92	277	0.99	1.00	0.99
Training	4	NU-F-1	104	0.95	1.00	1.00	117	0.99	0.89	0.65	96	0.51	0.99	0.89	77	0.78	1.00	1.00	309	0.99	0.99	0.99
Training	5	NU-M-4	120	0.78	0.99	0.96	89	0.63	1.00	0.97	215	0.94	0.98	0.95	28	0.89	0.96	0.47	321	1.00	0.93	0.91
Training	6	NU-F-2	128	0.98	0.99	0.95	0	nan	0.99	0.29	155	0.98	0.99	0.97	103	0.87	1.00	1.00	315	1.00	0.99	0.99
Training	7	NU-F-3	98	0.87	1.00	0.99	179	0.92	0.97	0.89	0	nan	0.98	0.00	214	0.87	0.97	0.92	289	1.00	1.00	1.00
Training	8	NU-M-5	146	0.97	0.97	0.91	28	0.71	0.96	0.45	169	0.76	0.98	0.93	32	0.91	0.98	0.73	301	0.99	0.99	0.99
Training	9	NU-F-4	217	0.98	0.98	0.93	236	0.88	0.96	0.86	211	0.96	0.98	0.90	224	0.78	0.99	0.94	293	1.00	0.99	0.98
Training	10	NU-M-6	113	0.92	0.94	0.70	157	1.00	0.96	0.85	141	0.64	1.00	0.99	106	0.77	0.99	0.92	324	1.00	0.99	0.99
Training	11	SRAL-F-H1	166	0.85	0.99	0.97	169	0.88	0.98	0.94	39	0.67	0.97	0.58	29	0.76	0.97	0.58	250	0.99	0.95	0.93
Training	12	SRAL-F-H4	114	0.86	0.92	0.70	42	0.81	0.98	0.69	0	nan	0.98	0.00	87	0.36	1.00	1.00	416	0.97	0.90	0.94
Training	13	SRAL-F-H6	114	0.88	0.98	0.89	166	0.84	1.00	1.00	0	nan	0.99	0.00	0	nan	0.98	0.00	443	0.97	0.93	0.96
Training	14	SRAL-M-H3	47	0.91	0.99	0.91	200	0.92	0.98	0.92	55	0.69	0.99	0.79	47	0.81	0.99	0.81	495	0.99	0.96	0.97
Training	15	SRAL2020BF	165	0.90	1.00	0.99	102	0.95	0.99	0.95	0	nan	0.99	0.00	0	nan	0.99	0.00	179	1.00	0.97	0.96
Training	16	SRAL2025M	163	0.91	0.99	0.97	121	0.88	0.99	0.94	116	0.80	0.99	0.97	0	nan	0.97	0.00	190	0.97	0.94	0.89
Training	17	SRAL2026F	43	0.70	1.00	1.00	0	nan	0.99	0.00	0	nan	0.97	0.00	0	nan	0.97	0.00	30	1.00	0.81	0.79
Training	18	SRAL2032BM	24	0.79	0.98	0.59	199	0.84	0.96	0.93	0	nan	0.94	0.00	30	0.80	0.96	0.56	310	0.86	0.98	0.98
Training	19	SRAL2019M	314	0.90	0.96	0.92	377	0.80	0.98	0.96	0	nan	0.98	0.00	0	nan	0.94	0.00	282	0.90	0.98	0.94
Training	20	SRAL2006M	255	0.85	0.95	0.92	73	0.85	0.98	0.83	0	nan	0.99	0.00	0	nan	0.99	0.00	310	0.94	0.92	0.91

Tab. S2. Detailed statistical information of the performance of the CNN model on subjects.
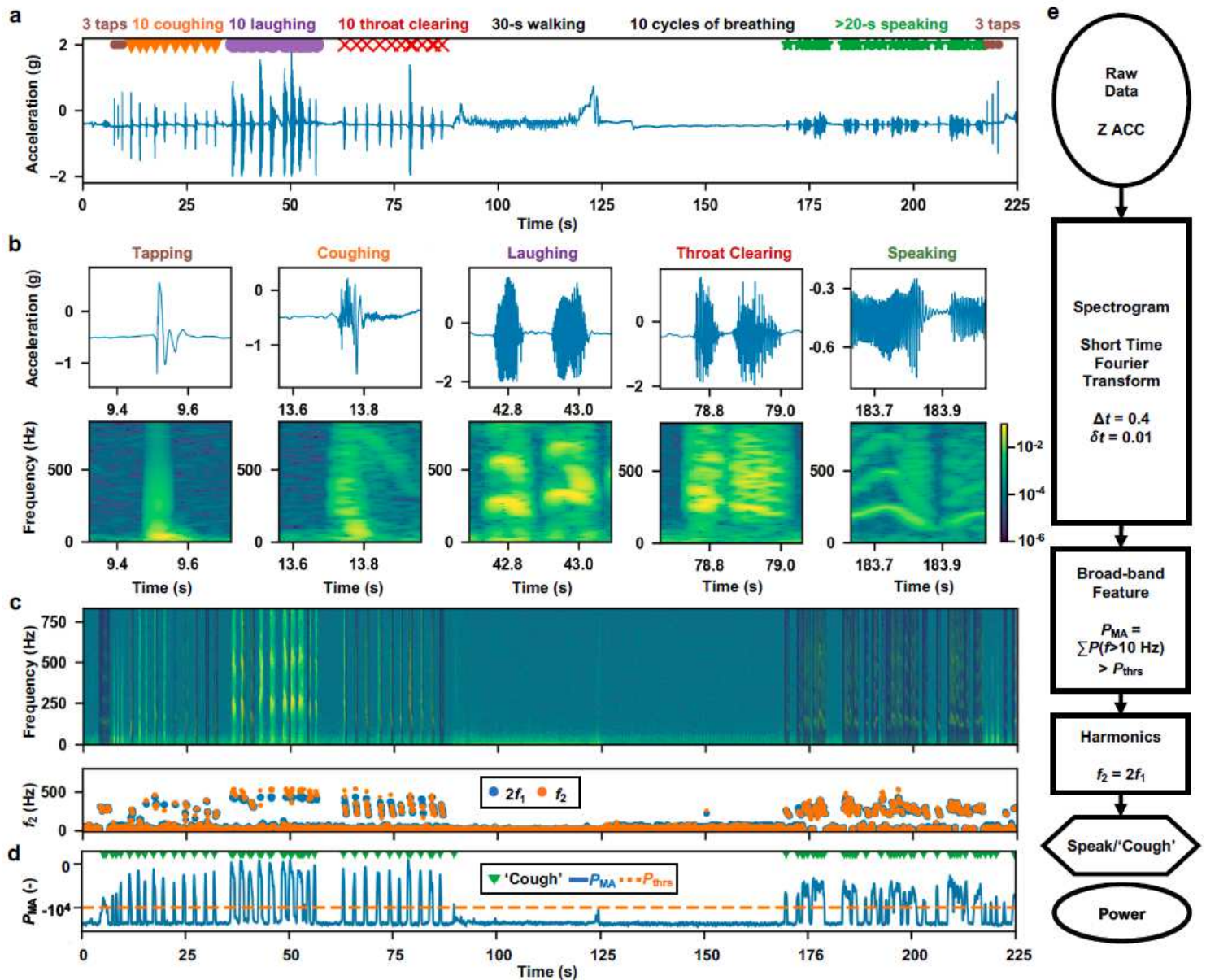
Figures

Figure 1

The health monitoring system incorporating a mechano-acoustic (MA) sensor, Bluetooth and cloudbased data transmission, automated data-processing platform and a user-interface with a minimum request for manual operation. (a) Schematics of the operational flow of the system that consists of a device, cloud,

and data processing platforms. (b) Sample three-axis acceleration raw data acquired continuously over 48 hours on a COVID-19 patient. Dashed lines indicate occurrences of various representative body processes of interest, shown in (c) zoomedin two-minute windows.

Figure 2

The signal preprocessing steps that identify broadband events of interest from the quiet and speaking time from mechano-acoustic (MA) measurements. (a) The raw z-axis data generated from controlled experiments on healthy normal subjects, with all the events of interest repeated in sequence following a designed protocol (See Methods for details). (b) Example 400-ms clips of the raw z-axis data and their corresponding spectrogram features. (c) Speaking signals distinct with a clear presence of harmonics (P(f1) and P(f2)) of fundamental frequencies f1 in the spectrogram analysis P(f), where 2f1 ≈ f2; See Ref. 43 for details). Detected speaking periods are shaded in blue in the spectrogram. (d) After excluding speaking time, the detection of the high-frequency (f > 10 Hz) MA power peaks with a minimum time

interval of 0.4 s and a threshold of -10000 yields time stamps for cough-like events that feature the impulse-like broad-band acoustics. (e) A flow diagram summarizing the preprocessing steps that take in the raw z-axis data and outputs the time stamps for cough-like and speaking events, along with their MA power, PMA.
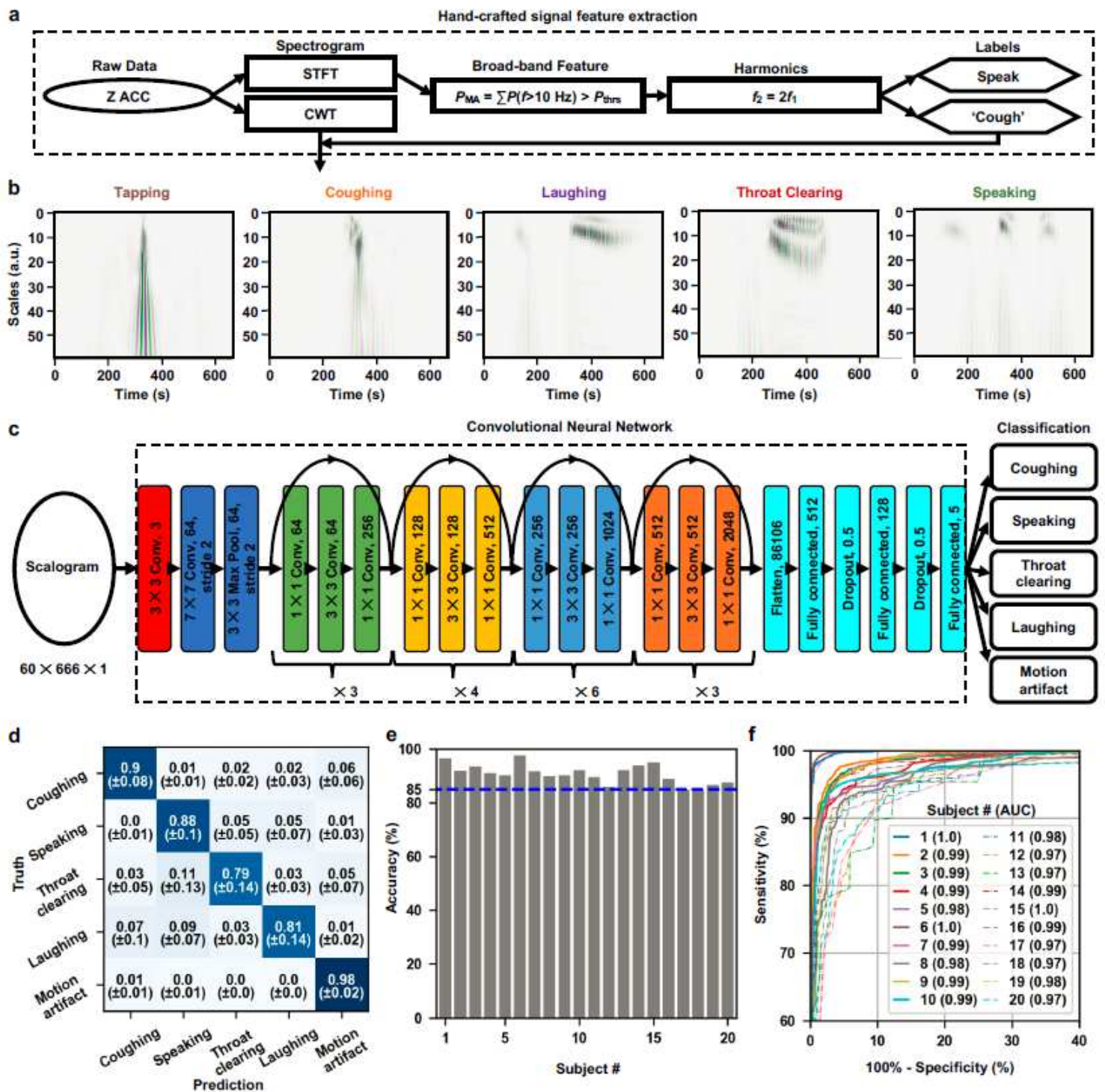

Figure 3

The machine learning algorithm for the classification of cough-like events extracted by the preprocessing algorithm. (a) Steps of feature scalogram generation from raw data. (b) Representative scalograms of

events of interest. (c) The architecture of a convolutional neural network that takes in a feature scalogram and outputs its probabilities of classes. (d) The averaged confusion matrix from the iterated 20 leave-one-out testings. (e) The overall testing accuracy on each left-out subject using a model trained on the other 19 subjects. (f) The macro-averaged Receiver Operating Characteristic (ROC) curves of each left-out subject using a model trained on the other 19 subjects and the corresponding Area under the Curve (AUC).
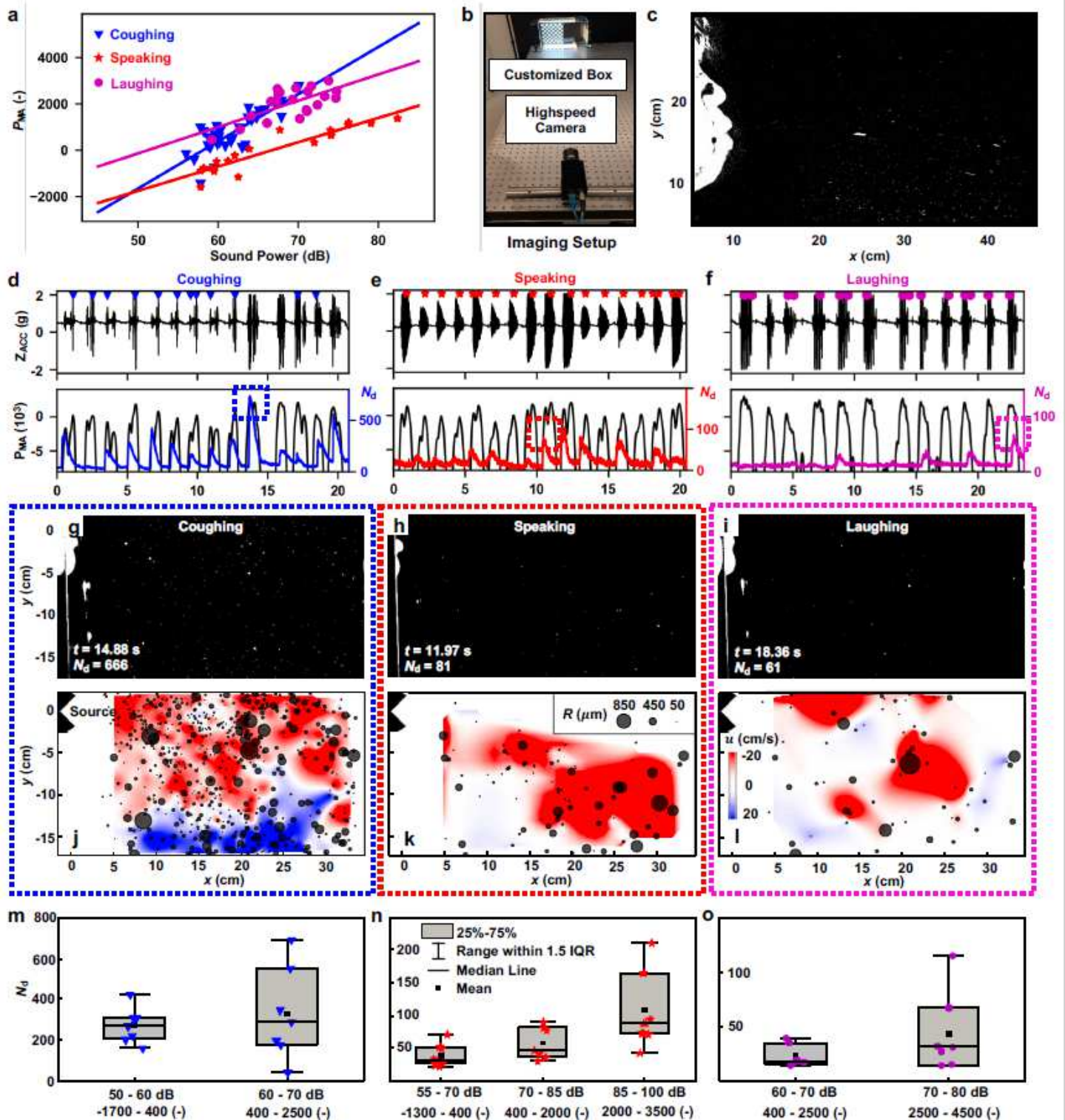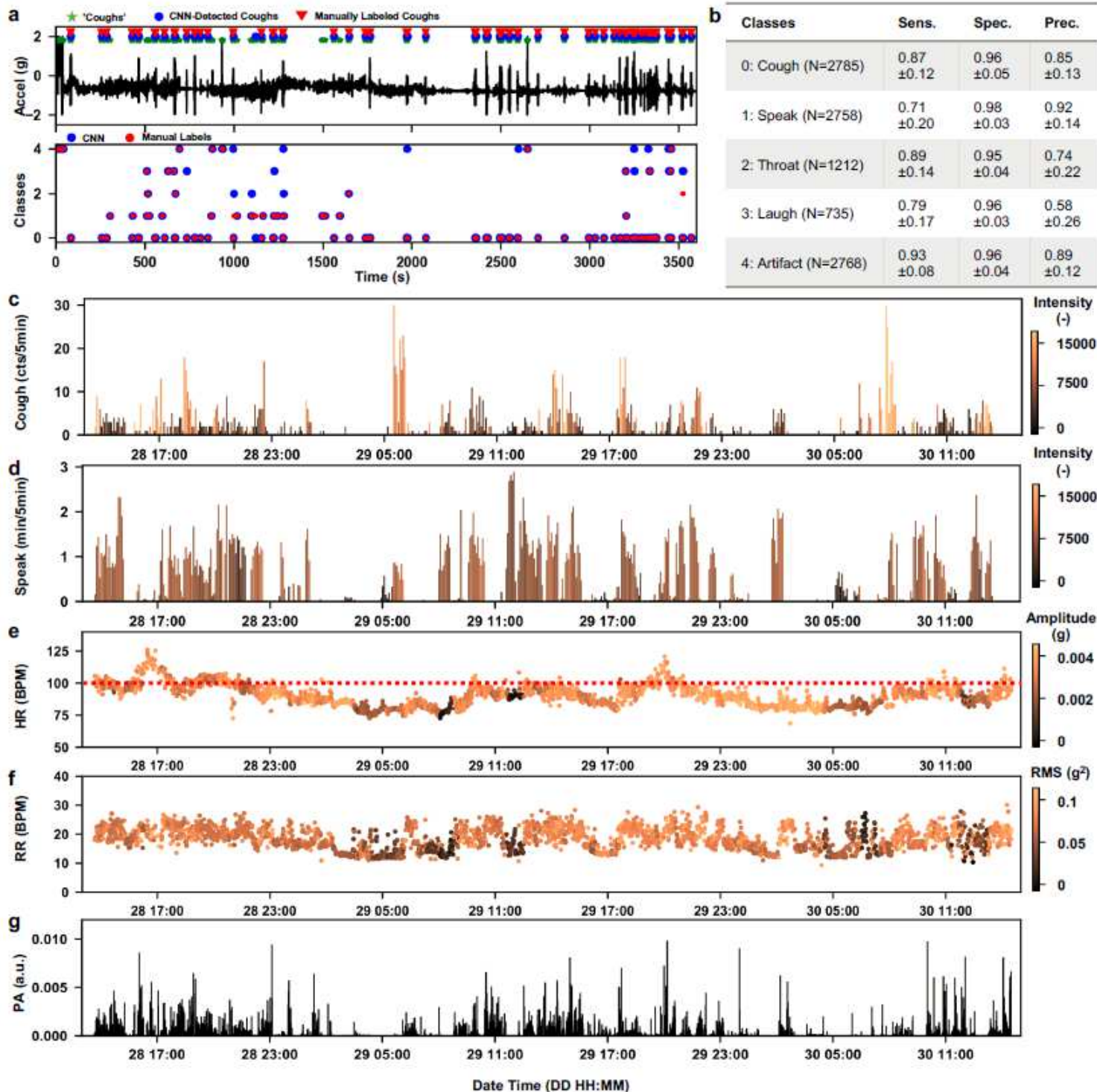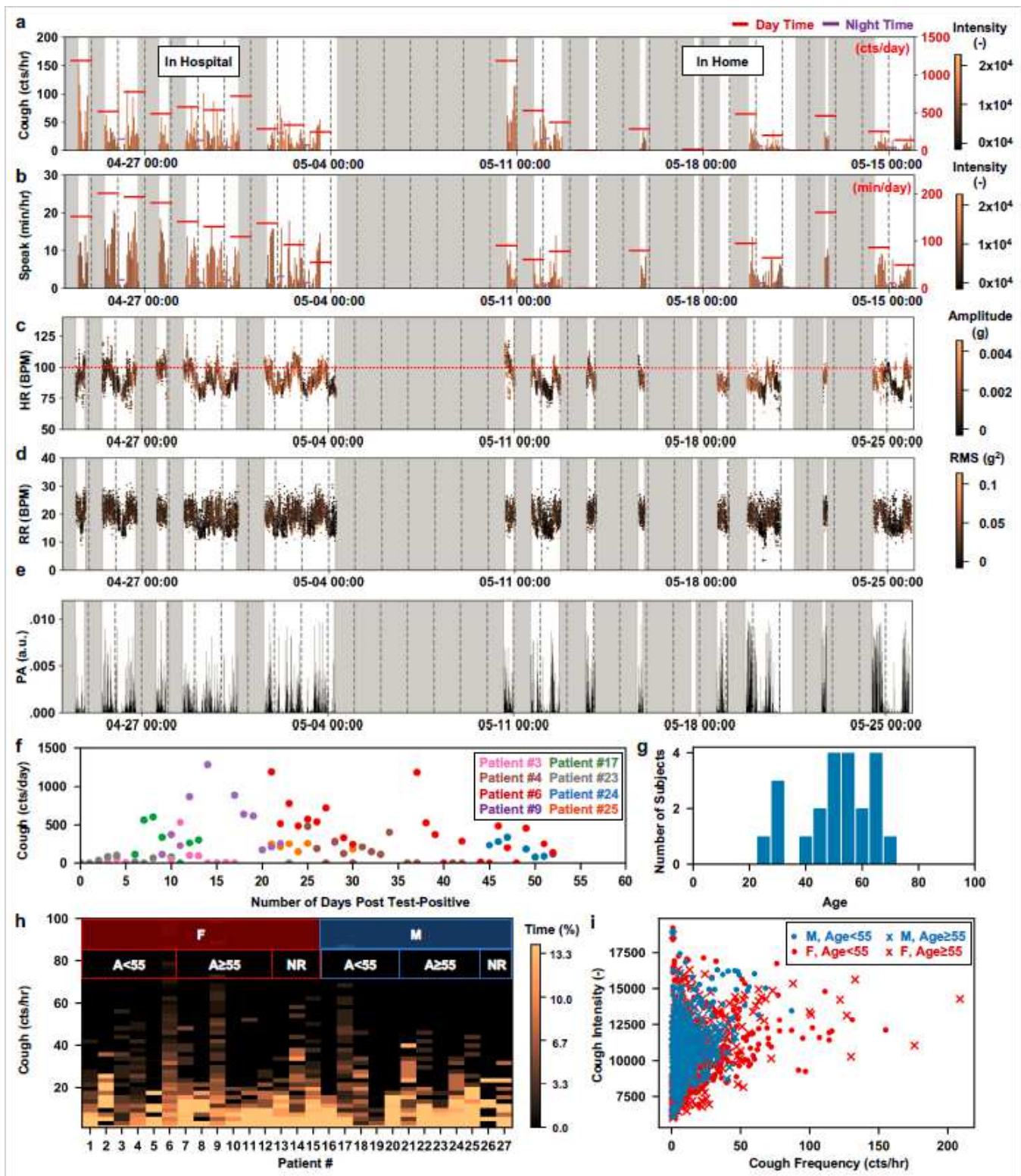

Figure 4

Mechano-acoustic sensing to quantify the transmission of droplets. (a) MA power vs. decibel meter measurement for coughing, speaking, and laughing. (b) Experimental setup for optical imaging of droplets. (c) Sample image of coughing. (d,e,f) Time series of MA z-axis data in sync with the analysis of MA power and the imaging detection of the number of the particles. (g,h,i) Instantaneous images of coughing, talking, and laughing at the peak of corresponding marked boxes in d,e,f. (j,k,l) Detected particles with sizes indicated by the diameters of the grey circular symbols, overlapped with velocity contour fields at the corresponding instances in g,h,i; the color denotes streamwise velocity in horizontal (x-axis) direction. (m,n,o) Box and whisker plots showing the number of particles for all measured cycles of coughing, speaking, and laughing, respectively. See Methods section for full description.

Figure 5

Deployment of MA device to the in-field COVID-19 patients. (a) Example one-hour raw z-axis acceleration data measured from a female patient. The automated algorithm detects cough-like events and outputs five-way classification for the events to coughing (0), speaking (1), throat clearing (2), laughing (3), and motion artifacts (4). (b) The macro-averaged testing performance (sensitivity/recall, specificity, and precision) of each type of events on the 10 patients with manual labels, which include 10,258 randomly sampled events in total. (c,d) Example results of the detected coughing and talking frequency and intensity (color-coded) in five-minute windows from continuous 48-hour monitoring of the same patient (raw acceleration data are shown in Fig. 1b-c). (e,f,g) The vital information, i.e., heart rate (HR), respiration rate (RR), and physical activity (PA), extracted from the same measurement, with their amplitude information color-coded.

Figure 6

Long-term monitoring of coughing and other biometrics of COVID-19 patients. Long-term mechanoacoustic sensing of (a) cough frequency per hour, (b) talk time per hour, (c) heart rate, (d) respiration rate, and (e) physical activity for the same patient shown in Fig. 5a, c-g, with the intensity or amplitude information of the associated events color-coded in each time bin. (f) The time series plot of coughing counts organized in days post the test-positive date from eights COVID-19 patients. (g) The age

distribution of the 27 patients whose data are not used to build the machine learning model. (h) The histogram of coughing frequency of the 27 patients. (i) The cough intensity versus cough frequency analyzed for each hour of data, clustered by four demographic groups.

Supplementary Files

This is a list of supplementary files associated with this preprint. Click to download.

- Video1.mp4